CR 114482

AVAILABLE TO THE PUBLIC

NATIONAL RESEARCH COUNCIL OF CANADA
CONSEIL NATIONAL DE RECHERCHES DU CANADA

NATIONAL AERONAUTICAL ESTABLISHMENT

LABORATORY TECHNICAL REPORT

RAPPORT TECHNIQUE DE LABORATOIRE

ÉTABLISSEMENT AÉRONAUTIQUE NATIONAL

OTTAWA. CANADA

NATIONAL AERONAUTICAL ESTABLISHMENT

ÉTABLISSEMENT AÉRONAUTIQUE NATIONAL

CANADA

PAGES / PAGES: 50

FIG. / DIAG.: 27

REPORT
RAPPORT

REPORT / RAPPORT: LTR-UA-14

DATE / DATE: July 1970

LAB. ORDER / COMM. LAB: NAE 1058

FILE / DOSSIER: M49-10N-5

SECTION

UNSTEADY AERODYNAMICS

FOR / POUR: Partially supported by the National Aeronautics and Space Administration, USA, under contract NASW-1947.

REFERENCE / RÉFÉRENCE

LTR-UA-14

STATIC AND DYNAMIC PITCHING MOMENT MEASUREMENTS ON A FAMILY OF ELLIPTIC CONES AT MACH NUMBER 11 IN HELIUM

SUBMITTED BY / PRÉSENTÉ PAR: K. Orlik-Rückemann
SECTION HEAD / CHEF DE SECTION

AUTHOR / AUTEUR: K. Orlik-Rückemann
J. G. LaBerge

APPROVED / APPROUVÉ: F. R. Thurston
DIRECTOR / DIRECTEUR

COPY NO. / COPIE NR. 6

ABSTRACT

Static and dynamic pitching moment measurements were made on a family of constant-volume elliptic cones about two fixed axes of oscillation in the NAE helium hypersonic wind tunnel at a Mach number of 11 and at Reynolds numbers based on model length of up to 14×10^6.

Viscous effects on the stability derivatives were investigated by varying the Reynolds number for certain models by a factor as large as 10. The models investigated comprised a 7.75° circular cone, elliptic cones of axis ratios 3 and 6, and an elliptic cone with conical protuberances.

TABLE OF CONTENTS

1.0 INTRODUCTION

No information is at present available on the dynamic stability of high lift-drag ratio configurations at hypersonic speeds. Such configurations, of course, are of immediate interest for application to some versions of the shuttle spacecraft and, at a later date, to the hypersonic aircraft. Information is needed to determine whether the dynamic stability of such vehicles can be provided by purely aerodynamic means or whether artificial stability devices have to be employed; in the latter case, knowledge of the inherent stability characteristics may be required for an optimum design of an artificial stability system.

To establish the significance of the problem, a flight mechanics analysis must be undertaken, based on a realistic set of aerodynamic characteristics of a typical configuration. For very simple geometrical shapes such as circular cones, such characteristics can usually be provided analytically without any difficulties. However, for more complex geometry, such as may result from a simultaneous consideration of requirements of high lift, low drag, satisfactory trim and static stability, and practical volume distribution, the analytical prediction of the aerodynamic characteristics, and particularly of those related to the unsteady flight conditions, may become very complicated or else not too accurate. However, the aerodynamic characteristics may also be obtained experimentally, for example, by static and dynamic tests in a hypersonic wind tunnel. Once a suitable experimental technique has been developed and checked out on simple models, the same procedure may be used for obtaining data on a wide variety of configuration geometry.

This report presents the results of dynamic experiments performed on a series of elliptic cones in a hypersonic helium wind tunnel. The experiments consisted of oscillation in-pitch about two axes and were performed at Mach number 11 in a wide range of Reynolds numbers. Recently-constructed experimental equipment was employed, which is particularly suitable for testing hypersonic lifting configurations. The models were selected in such a way that they were of a simple enough geometry to later permit analytical calculations and at the same time had lift-drag ratios representative of typical hypersonic configurations of practical interest. Three of the models chosen had previously been tested elsewhere and their steady aerodynamic characteristics at supersonic speeds were known.

2.0 MODELS

2.1 Geometry

The models investigated constituted a constant-volume family, viz., all were of the same length and base area, see Fig. 1. Three of the models were geometrically similar to those of Ref. 1 and consisted of a circular cone and two elliptic cones of increasing eccentricity. The fourth body was basically of an elliptic cross-section but carried conical protuberances at the top and bottom, the profile being given by a fourth order even cosine Fourier series. A body of this cross-section had been employed at the NAE for supersonic and hypersonic flow field investigations on conical bodies (Ref. 2).

The scale of the models was chosen such that the largest major diameter was still within the diameter of the inviscid core of the nozzle test section. Model designation followed that of Ref. 1 with the further designation of B7 given to the Fourier body.

2.2 Model Construction

Except for the circular cone, a computer-programmed milling machine was used to produce the external and internal profiles. Details of a typical model are given in Fig. 2. The internal surface was machined first and this was done in the following manner: The model was slit along the major axis up to the solid forebody and the two halves were milled out, the final finish being that produced by the milling cutter. The two portions were then silver-soldered, the external profile cut and the final finish obtained by hand-polishing. The base of the solid forebody was then milled flat and adaptor mounting holes were tapped into the base. Local internal pads were left at the rear of the shells of models B1, B3 and B4 for attachment of brackets connecting the models to the driving mechanism.

A photograph of the completed models is shown in Fig. 3.

2.3 Model Mounting

Details of model mounting is given in Ref. 3 which describes the new dynamic stability apparatus that was used for this investigation. One of the stings and the adaptors for the two axes of oscillation are shown in Fig. 4; the adaptors above the sting relate to model B1, those below to the other models. The dimensional relationship between model, sting and sting support are given in Fig. 5. The general mounting arrangement in the tunnel nozzle is shown in Fig. 6, while detailed views of the model installation in the test section are given in Figs. 7, 8 and 9.

3.0 WIND TUNNEL

The tests were performed in the helium hypersonic wind tunnel facility described in Ref. 4, at a nominal Mach number of 11. The nozzle used had a test-section diameter of 11 inches and an inviscid core diameter of at least 6 inches. A photograph of the wind tunnel is shown in Fig. 10.

The stagnation pressure was varied through a maximum range of about 150 to 1600 psia giving a Reynolds number variation of about 1.5 to 14 x 10^6 based on body length. The resulting Mach number distribution in the plane of model oscillation at three longitudinal stations in the nozzle is given in Fig. 11. The variation of the mean Mach number at the test-section centre line with stagnation pressure is shown in Fig. 12.

The helium was pure to within 99.996 percent (by volume) or better.

4.0 EXPERIMENTAL EQUIPMENT AND PROCEDURE

A new wind tunnel apparatus for dynamic stability experiments, described in detail in Ref. 3, was used for the measurements. In this apparatus the model is sting-mounted from the rear and attached to the sting by means of miniature frictionless flexural pivots. The main stiffness of the oscillatory system is provided by a pair of gimbal springs mounted on the outside of either sidewall of the tunnel and attached (via another flexural pivot) to the base of the model by pre-stressed piano wires. A specially designed electromagnetic driver imparts the oscillatory motion to one of the springs, while a linear variable displacement transducer records the motion of the other spring. The main advantage of the new apparatus is that it requires only very little space inside the model and hence permits testing of very slender models. A schematic of the apparatus mounted in the NAE helium wind tunnel is shown in Fig. 6.

The frequency and logarithmic decrement were obtained from Dampometer readings using the method of free oscillation with automatically recycled feedback excitation described in Ref. 5. The plane of oscillation was parallel to the minor axis of the model. Two positions of the axis of oscillation were used, one at 50 percent of the model length from the apex and the other at 65.3 percent. These positions were obtained using two stings and two adaptors of different lengths which kept the model in the same position relative to the test section and also relative to the sting support. The actual centre of gravity of all the models was located between the two axes of oscillation.

All tests were performed at a model mean incidence of zero degrees. Maximum amplitude of oscillation was $\pm 1.5^{\circ}$ with measurements being made during amplitude decay from $\pm 1^{\circ}$ to $\pm 0.5^{\circ}$. Test frequencies varied from 33 to 41 Hz (k=0.013 to 0.016) depending on model, axis position and stagnation pressure.

Model base pressure, test-section pitot pressure and tunnel stagnation pressure were measured with pressure transducers located outside the tunnel. Stagnation temperature (approximately room temperature) was measured with a copper-constantan thermocouple in the centre of the settling chamber. The output of these instruments were registered on strip chart potentiometer recorders.

Run duration varied from about 5 to 10 seconds depending on the rate of model damping (i.e. depending on the particular model and stagnation pressure), one damping cycle taking place per run. Ten wind-off tare readings were taken immediately before and after each run when the tunnel was a low pressure.

The output of the motion transducer (see Ref. 3) was also fed to an oscillograph (Visicorder) to ascertain that, for all practical purposes, the damping was constant in the amplitude range being investigated. The pitot pressure was also registered on another channel of the oscillograph to ensure that the tunnel flow uniformity was satisfactory during the period of damping measurement. Another oscillograph (Sanborn) was used for recording (to a much smaller scale) the motion trace during the initial setting up when the model or axis of oscillation was changed.

In order to assess the effect of the sting cross-sectional area on the results, the dimension of the sting in the plane of oscillation was increased by bonding two strips of lucite along the flat sides of the sting. This increased the cross-sectional area from 0.42 to 0.70 in.^{2}, i.e., by 2/3. The effect of this increase was found to be within the scatter of the results for both the base pressure ratio and the derivatives.

The sting was observed to oscillate slightly during the experiments. This motion was then measured using strain gauges bonded to the sting. The sting oscillation was found to be practically the same during the calibration and wind-on conditions, had the same phase and frequency as the model oscillation and produced an effective shift rearward of the axis of oscillation. This shift was so small that no correction of axis position itself was deemed necessary; however, it affected the statically-calibrated value of the angular mechanical stiffness of the system by about 5 percent, which was taken into account in the data reduction.

In the present experimental apparatus the pitching oscillation of the model was excited by imparting a translational oscillation to the system along an axis normal to the longitudinal axis of the tunnel. This oscillation in turn induced vibrations of the nozzle structure which were evident when the apparatus was first installed. The effect of these vibrations was to increase the tare damping of the system and to degrade the repeatability of the damping. This interference was reduced considerably by rotating the nozzle about its longitudinal axis to an optimum angular position, by adding lateral supports to the tunnel structure and by modifying the nozzle mass distribution by the addition of lead weights. A further refinement was achieved by introducing hard rubber gaskets between the gimbal springs and the nozzle wall and between the downstream flange of the nozzle and the upstream flange of the diffuser. With these improvements the vibration effects were reduced to an acceptable level.

5.0 DATA REDUCTION

The definitions and derivations given in this section are similar to those in Ref. 6, but are reproduced here for convenience.

5.1 Static and Dynamic Derivatives

The expressions for static and dynamic pitching moment derivatives are, respectively, as follows

$$C_{m_\theta} = \frac{\partial C_m}{\partial \theta} = \frac{2M_\theta}{\rho V^2 S\ell} = -\frac{8\pi^2 I(\nu^2 - \nu_o^2)}{\rho V^2 S\ell} \qquad (1)$$

$$C_{m_{\dot\theta}} = \frac{\partial C_m}{\partial\left(\frac{\ell\dot\theta}{2V}\right)} = \frac{4M_{\dot\theta}}{\rho V S\ell^2} = -\frac{8I}{\rho V S\ell^2}\left[\delta\nu - \frac{\delta_o\nu_o}{2}\left(1 + \frac{\nu_o}{\nu}\right)\right] \qquad (2)$$

where

$$C_m = \frac{M}{\frac{1}{2}\rho V^2 S\ell}$$

M	=	pitching moment
$\frac{1}{2}\rho V^2$	=	free-stream dynamic pressure
S	=	base area of model
ℓ	=	model length
I	=	moment of inertia of oscillating system
$\theta, \dot\theta$	=	angle of oscillation in pitch about a fixed axis, and its first derivative with respect to time.
δ	=	logarithmic decrement
ν	=	oscillation frequency, Hz
$(\ )_o$	=	vacuum condition

The terms in the square bracket of Eq. (2) indicate that the damping is assumed to be viscous and hysteretic in equal proportions (see discussion in Ref. 7).

Eqs. (1) and (2) were programmed for computation using an IBM OS 360/50 CPS facility.

With pitching moment results available for two axes of oscillation the corresponding lift derivatives can be calculated, as shown in paragraph 5.2. The static and dynamic lift derivatives are defined as follows.

$$C_{L_\theta} = \frac{\partial C_L}{\partial \theta} = \frac{2L_\theta}{\rho V^2 S} \qquad (3)$$

$$C_{L_{\dot\theta}} = \frac{\partial C_L}{\partial \left(\frac{\ell\dot\theta}{2V}\right)} = \frac{4L_{\dot\theta}}{\rho V S \ell} \qquad (4)$$

where

$$C_L = \frac{L}{\frac{1}{2}\rho V^2 S}$$

L = lift force

The reduced frequency of the motion is defined as

$$k = \frac{\omega \ell}{2V} = \frac{\pi \nu \ell}{V} \qquad (5)$$

where ω = circular frequency, rad./sec.

For $\gamma = 5/3$, $T_o = 540^\circ R$, $M_\infty \geq 7$ and with ℓ expressed in inches, Eq. (5) reduces to

$$k \approx 4.5 \times 10^{-5} \; \nu \ell \qquad (6)$$

5.2 Axis Transfer Equations

When the first-order* pitching moment derivatives (C_{m_θ} and $C_{m_{\dot\theta}}$) are known about two axes, it is possible to determine the corresponding first-order lift derivatives (C_{L_θ} and $C_{L_{\dot\theta}}$) and to calculate the first-order moment derivatives about any other axis, provided the frequency effects are negligible.

Consider three axes "1", "2" and "3" starting from the rear of the body, at distances x_1, x_2 and x_3, respectively, from the apex, the distance between successive axes being expressed

---

* first order with respect to frequency.

as x_{32} and x_{21}, and x_{13} being defined as $x_{13} = -(x_{32} + x_{21})$.
We have, from Ref. 6:

$$C_{m_{\theta_2}} = C_{m_{\theta_1}} - \frac{x_{21}}{\ell} C_{L_\theta} \tag{7}$$

$$C_{m_{\dot\theta_2}} = C_{m_{\dot\theta_1}} - \frac{x_{21}}{\ell} C_{L_{\dot\theta_1}} + \frac{2x_{21}}{\ell} C_{m_{\theta_1}} - 2\left(\frac{x_{21}}{\ell}\right)^2 C_{L_\theta} \tag{8}$$

$$C_{L_{\theta_2}} = C_{L_{\theta_1}} = C_{L_\theta} \tag{9}$$

$$C_{L_{\dot\theta_2}} = C_{L_{\dot\theta_1}} + \frac{2x_{21}}{\ell} C_{L_\theta} \tag{10}$$

$$\frac{x_{32}}{\ell} C_{m_{\dot\theta_1}} + \frac{x_{13}}{\ell} C_{m_{\dot\theta_2}} + \frac{x_{21}}{\ell} C_{m_{\dot\theta_3}} = 2\,\frac{x_{32}x_{21}x_{13}}{\ell^3} C_{L_\theta} \tag{11}$$

By letting axis '3' be at the apex, the derivatives about this position can be obtained.

5.3 Correction for Spring Surging

The effect of spring surging, discussed in Ref. 3, was found to increase the value of $C_{m_{\dot\theta}}$ and C_{m_θ} by about 0.4 percent.

6.0 RESULTS

All the results are listed in Table 1. Typical amplitude decay curves for tare calibrations and runs at various stagnation pressures obtained from the oscillograph records are shown in Fig. 13; these indicate that the damping was indeed quite constant within the amplitude range investigated.

6.1 Effect of Reynolds Number

The derivatives $(-C_{m_\theta})$ and $(-C_{m_{\dot\theta}})$ for all four models and for two axis positions on each model, are plotted in Figs. 14 to 17 as functions of the free-stream Reynolds number.

The base pressure for all models is given in Fig. 18, again as a function of the free-stream Reynolds number.

For an easier assessment of the effect of Reynolds number, the data of Figs. 14 to 18 are combined for each model in Figs. 19 to 22, inclusive.

6.2 Effect of Cross-Sectional Axis Ratio

The derivatives $(-C_{m_\theta})$ and $(-C_{m_{\dot\theta}})$ for highest value of the Reynolds number are plotted for all the models and for both axis positions on each model in Fig. 23 as functions of cross- sectional axis-ratio.

The pitching moment derivatives about the apex and for the same Reynolds number as above are plotted against the cross-sectional axis ratio in Fig. 24. A similar plot for the lift derivatives C_{L_θ} and $C_{L_{\dot\theta}}$ is shown in Fig. 25. In calculating the apex derivatives it was assumed that the axis transfer equations of paragraph 5.2 applied since, for the present low values of the reduced frequency, the effect of second order derivatives, which was discussed in Ref. 6, can be considered negligible.

7.0 DISCUSSION

7.1 Reliability of Results

As partly mentioned in the preceding paragraphs, several possible sources of experimental error were carefully examined. This included the possible effects of sting interference, sting oscillation, tunnel vibration and spring surging. Some of these effects were found to be within experimental scatter; for others corrective measures were introduced. In addition, the effect of lateral loads on flexure pivots (such as could result from the aerodynamic drag on the model) on the calibration values of the apparatus stiffness and damping was measured and found negligible. The effect of the flow on the model support wires was kept to a minimum by the use of wedge-shaped cantilever wire shields (not shown on Fig. 6) mounted on the walls. Possible errors in pressure readings were controlled by recording several pressures and verifying their ratios. The purity of helium was monitored and found always within acceptable limits. The amplitude range for which the free oscillation results were representative was carefully controlled and always maintained at a constant value. In addition to the automatic data processing, the time-histories of at least two oscillation decays for every model and axis-position combination were also analyzed manually, confirming that in all cases the damping was fairly constant in both the calibration and tunnel-run conditions. Finally, as mentioned before, precautions were taken to render the effect of axis position independent of the model location in the tunnel and of the model-sting configuration by retaining the model always in the same position with regard to both the test section and the sting support. Thus the results obtained and their variation with Reynolds number and with the axis position for the different models appear trustworthy. However, as always with this type of experiment, a certain level of scatter must be accepted due to the inevitable presence of flow fluctuations and structural vibrations. Some scatter could also be attributed to the presence of a transitional (and hence not strictly repeatable from run to run) boundary layer on the models in certain experimental conditions.

7.2 Effect of Reynolds Number

Experiments on model B1 were carried out within the full available range of Reynolds number, which, at a nominal Mach number of 11, was between 1.5 and 14 million for a 9 inch model. The resulting variation with Reynolds number of the derivatives C_{m_θ} and $C_{m_{\dot\theta}}$ and the base pressure ratio p_b/p_∞ (see Fig. 19) may be compared with similar data*, reported in Refs. 8 and 9, for a 10^o semi-angle cone at supersonic and hypersonic Mach numbers in air. It was shown there that the occurrence of boundary layer transition at the base of a cone could be determined by studying the variation of the cone base pressure ratio with Reynolds number. As long as the boundary layer over the entire model remained laminar, the base pressure ratio was found to decrease with increasing Reynolds number. Transition at the model base was generally found to occur at a value of Reynolds number slightly less that that at which the base pressure ratio first began to level off. At lower Mach numbers this onset of transition was also associated with the occurrence of a maximum value in the variation of the derivative $(-C_{m_{\dot\theta}})$ with $Re_{\infty,\ell}$, and a minimum value in the corresponding variation in the derivative $(-C_{m_\theta})$. At higher Mach numbers the development of these maximum and minimum values was shifted towards higher Reynolds number.

The variation of the present results for model B1 with Reynolds number, as shown in Fig. 19, shows the same characteristic trends as discussed above; on that basis and taking into account that the Mach number of the present experiments was as high as 11, it may be expected that the onset of boundary layer transition at the base of model B1 probably occurred at the value of $Re_{\infty,\ell}$ some-

---

* It may be noted that our notation C_{m_θ} and $C_{m_{\dot\theta}}$ is equivalent to the notation C_{m_α} and $(C_{m_q}+C_{m_{\dot\alpha}})$, respectively, of these references, if the latter are based on the model length.

where between 3 and 4 million*. Hence only the data points obtained at the lowest two values of $Re_{\infty,\ell}$ may be considered representative of a laminar boundary layer over the entire cone; the remaining points represent a boundary layer which is partly laminar, partly transitional and possibly partly turbulent. At the highest value of $Re_{\infty,\ell}$ the results obtained should be approaching those which might be expected for inviscid flow conditions.

On elliptic cones the main contribution to the pitching moment comes from the central regions of the upper and lower surfaces, rather than from the areas on the sides. For cones of constant length and volume, the flatter the cone, the smaller is the flow deflection in these regions and the higher is the corresponding local Mach number, as shown in Fig. 26. Assuming that the boundary layer transition on elliptic cones occurs at approximately the same local Mach numbers as on circular cones, the average local transition Reynolds numbers in the central regions of models B3, B4 and B7 may be slightly higher (say 10 to 20 percent) than on model B1. Since also the average ratio of the local to the free-stream Reynolds number is slightly lower for these models (see Fig. 27), it follows that the average free-stream transition Reynolds number for models B3, B4 and B7 may be higher by some 20 to 60 percent than the corresponding figures for model B1. Hence the transition at the base of those models probably occurs at free-stream Reynolds numbers not exceeding 5 to 6 million. Thus practically all the results obtained for models B3, B4 and B7 represent transitional or even turbulent flow conditions in the vicinity of the model base. However, except for the results for model B3 at the forward axis position, no significant variations in the $(-C_{m_{\dot{\alpha}}})$-curve, such as were observed for model B1, can be distinguished.

---

* This also agrees very well with the summary plot of Ref. 11, which for the present conditions of a local Mach number of 7.43 and a unit local Reynolds number of 0.57 million predicts a $(Re_{\infty})_{transition}$ of 3.4 million. (The ratio of the local to the free-stream Reynolds number is taken here as 1.47 - see Fig. 27).

For the axis positions used in this investigation the effect of dynamic viscous pressure interaction (see Ref. 10) may be expected to reduce the values of derivative $(-C_{m_{\dot\theta}})$ as long as most of the cone* is in a fully laminar or fully turbulent boundary layer. In each of these cases the effect should, of course, become smaller as the thickness of the boundary layer decreases. This is confirmed by the present results where derivative $(-C_{m_{\dot\theta}})$ is seen to increase with Reynolds number in two representative cases: (a) for model B1 at the two lowest values of $Re_{\infty,\ell}$, when the flow is expected to be laminar over the entire cone and (b) for models B4 and B7 at the higher end of the $Re_{\infty,\ell}$-range where the flow is expected to be turbulent over the rear portion of the cone.

It may be expected that the effect of transitional boundary layer will be more pronounced for forward positions of the axis of oscillation where the moment arm to the important region close to the model base is the largest. This is well illustrated by the results for models B1 and B3, where a well-defined peak in the $(-C_{m_{\dot\theta}})$-curve is clearly visible for the forward axis position. A similar but smaller peak appears for the rearward axis position for model B1. However, no such effect can be distinguished for the rearward axis position for model B3. In view of this, the sharpness of the corresponding peak for the forward axis position for that model is quite surprising. No explanation can be offered at the present time.

Except for model B1, where the $(-C_{m_\theta})$-curve exhibits a minimum in the same general range of Reynolds number in which the $(-C_{m_{\dot\theta}})$-curve goes through a maximum, (and which agrees with the previously-cited references), no significant variation with Reynolds number can be distinguished in the $(-C_{m_\theta})$-curve for the remaining models.

* In this connection the rear part of the cone is the most important, partly because of the larger area and partly because of the thicker boundary layer.

7.3 Effect of Cross-Sectional Axis-Ratio

Because of rather large effects of Reynolds number on some of the results obtained and because of the different way in which these effects manifested themselves for different models, no general cross-plotting of the results as functions of the cross-sectional axis-ratio was considered practical. Since however, as previously mentioned, the results obtained at the highest value of Reynolds number could be considered as approaching the inviscid values, such a cross-plotting was undertaken for that particular set of results. It may be seen in Fig. 23 that the derivative $(-C_{m_{\dot{\theta}}})$ for both experimental axis positions and the derivative $(-C_{m_{\theta}})$ for the forward axis position increase with the cross-sectional axis-ratio, while the derivative $(-C_{m_{\theta}})$ for the rearward axis position shows a slight decrease. The results for model B7 are also included in Fig. 23 and exhibit good agreement with the curve for the elliptic cones in the case of derivative $(-C_{m_{\theta}})$; however, the values of derivative $(-C_{m_{\dot{\theta}}})$ are somewhat higher than those which would be expected for a strictly elliptic cone with the same cross-sectional axis-ratio.

From the experimental pitching-moment derivatives the static and dynamic lift-force and pitching-moment derivatives about the cone apex were calculated, using axis transfer equations listed in paragraph 5.2. The results are plotted in Fig. 24 and 25 and show in all cases (including model B7) a smooth increase with cross-sectional axis-ratio.

8.0 REFERENCES

1. Jorgensen, L. H. — Elliptic Cones Alone and with Wings at Supersonic Speeds. NACA Report 1376, 1958.

2. Jones, D. J. — Numerical Solutions of the Flow Field for Conical Bodies in a Supersonic Stream. CASI Transactions, No. 1, V.3, p. 62, March 1970.

3. Orlik-Rückemann, K.J., LaBerge, J. G., Adams, P. A., Conlin, L. T. — A Wind Tunnel Apparatus for Dynamic Stability Experiments on Sting-Mounted Slender Bodies. NRC LTR-UA-13, March 1970.

4. Orlik-Rückemann, K.J., LaBerge, J. G. — NAE Helium Hypersonic Wind Tunnel. NRC Quarterly Bulletin, DME/NAE 1965(3), pp. 1-31, 1 July - 30 September 1965.

5. Orlik-Rückemann, K.J. — Measurement of Aerodynamic Damping and Stiffness Derivatives in Free Oscillation with Automatically Recycled Feedback Excitation. NRC, NAE Aero Report LR-246, June 1959.

6. Orlik-Rückemann, K.J., LaBerge, J.G. — Static and Dynamic Longitudinal Stability Characteristics of a Series of Delta and Sweptback Wings at Supersonic Speeds. NRC, NAE Aero Report LR-396, January 1966.

7. Orlik-Rückemann, K.J. — Wind Tunnel Measurements of Dynamic Derivatives. Second Edition. Lecture Notes, UCLA, August 1963.

8. Schueler, C. J.; Ward, L. K.; Hodapp Jr., A. E. — Techniques for Measurement of Dynamic Stability Derivatives in Ground Test Facilities. Agardograph 121, October 1967.

9. Ward, L. K.; Uselton, B. L. — Dynamic Stability Results for Sharp and Blunted 10-Deg Cones at Hypersonic Speeds. AEDC-TR-68-277, December 1968.

10. Orlik-Rückemann, K.J. — Dynamic Viscous Pressure Interaction in Hypersonic Flow. NRC, NAE Aero Report LR-535 (to be published).

11. Maddalon, D.V.; Henderson Jr., A. — Boundary-Layer Transition on Sharp Cones at Hypersonic Mach Numbers. AIAA J. V. 6, No. 3, pp. 424-431, March 1968.

TABLE 1

EXPERIMENTAL RESULTS

MODEL	$\bar{x}_o$	p_o (PSIA)	M_∞	$Re_{\infty,\ell}$ $\times 10^{-6}$	p_b/p_∞	p_o'/p_o	ν (HZ)	$-C_{m_{\dot\theta}}$	$-C_{m_\theta}$
B1	0.50	151	10.5	1.57	0.902	0.01741	38.9	0.095	0.349
		152	10.5	1.57	0.892	0.01763	38.9	0.065	0.349
		152	10.5	1.57	0.881	0.01835	38.7	0.087	0.355
		154	10.5	1.57	0.865	0.01747	38.9	0.105	0.352
		290	10.8	2.88	0.585	0.01855	38.8	0.207	0.375
		294	10.8	2.92	0.558	0.01820	38.8	0.199	0.370
		303	10.8	2.97	0.602	0.01808	39.1	0.269	0.369
		311	10.8	2.99	0.578	0.01804	39.1	0.247	0.370
		429	11.0	4.14	0.464	0.01765	39.1	0.464	0.351
		445	11.0	4.27	0.469	0.01804	38.9	0.480	0.354
		608	11.1	5.67	0.453	0.01730	39.1	0.468	0.357
		797	11.3	7.29	0.439	0.01691	39.2	0.580	0.336
		804	11.3	7.38	0.418	0.01695	39.2	0.572	0.337
		992	11.5	8.97	0.433	0.01643	39.5	0.611	0.356
		1093	11.5	9.81	0.435	0.01617	39.6	0.434	0.370
		1382	11.7	12.24	0.428	0.01553	39.9	0.321	0.408
		1614	11.8	14.19	0.413	0.01525	40.0	0.366	0.377
B1	0.653	153	10.5	1.57	0.842	0.01830	33.7	0.160	0.049
		296	10.8	2.93	0.568	0.01818	33.8	0.222	0.051
		600	11.1	5.62	0.450	0.01737	33.8	0.373	0.027
		799	11.3	7.32	0.431	0.01685	33.8	0.434	0.017
		802	11.3	7.38	0.445	0.01698	33.8	0.447	0.021
		999	11.5	9.00	0.458	0.01641	33.9	0.390	0.040
		1210	11.6	10.80	0.433	0.01593	34.0	0.258	0.067
		1398	11.7	12.33	0.429	0.01552	34.1	0.246	0.065
		1618	11.8	14.22	0.411	0.01515	33.9	0.252	0.038
B3	0.50	392	10.9	3.78	0.523	———	38.8	0.421	0.635
		398	10.9	3.82	0.512	0.01771	38.8	0.366	0.610
		590	11.1	5.58	0.479	0.01773	39.2	0.340	0.643
		595	11.1	5.60	0.479	0.01768	39.3	0.408	0.647

TABLE 1 - CONTINUED

MODEL	$\bar{x}_o$	P_o (PSIA)	M_∞	$Re_{\infty,\ell}$ $\times 10^{-6}$	P_b/P_∞	P_o'/P_o	ν (HZ)	$-C_{m_{\dot{\theta}}}$	$-C_{m_\theta}$
B3	0.50	611	11.2	5.76	0.475	0.01763	39.3	0.367	0.648
		807	11.3	7.38	0.459	0.01716	39.5	0.486	0.651
		892	11.4	8.10	———	0.01697	39.6	0.580	0.642
		991	11.5	8.95	0.439	0.01674	39.7	0.703	0.644
		1037	11.5	9.36	———	0.01677	39.8	0.839	0.648
		1042	11.5	9.36	0.446	0.01683	39.8	0.836	0.653
		1052	11.5	9.45	0.444	0.01653	39.8	0.821	0.642
		1141	11.6	10.21	0.435	0.01631	39.9	0.547	0.638
		1184	11.6	10.53	0.439	0.01652	40.0	0.522	0.653
		1387	11.7	12.28	0.432	0.01582	40.2	0.542	0.639
		1618	11.8	14.04	0.429	0.01578	40.7	0.509	0.653
		1630	11.8	14.31	0.430	0.01570	40.6	0.488	0.644
B3	0.653	611	11.2	5.76	0.492	0.01728	33.9	0.378	0.046
		814	11.3	7.51	0.467	0.01697	33.9	0.403	0.037
		991	11.5	8.95	0.468	0.01679	33.8	0.410	0.029
		996	11.5	8.97	0.458	0.01668	33.8	0.418	0.028
		1106	11.5	9.90	0.464	0.01648	33.8	0.418	0.024
		1136	11.6	10.21	0.460	0.01638	33.8	0.423	0.023
		1194	11.6	10.66	0.459	0.01634	33.8	0.437	0.020
		1255	11.6	11.16	———	0.01619	33.8	0.430	0.016
		1420	11.7	12.56	0.460	0.01578	33.8	0.431	0.012
		1651	11.9	14.49	0.450	0.01526	33.8	0.451	0.008
B4	0.50	991	11.5	8.95	0.465	0.01665	39.3	0.490	0.847
		1111	11.5	9.99	0.468	0.01639	39.5	0.514	0.849
		1210	11.6	10.80	0.474	0.01621	39.7	0.486	0.857
		1238	11.6	11.03	0.463	0.01611	39.7	0.546	0.852
		1324	11.6	11.74	0.466	0.01600	39.9	0.534	0.854
		1397	11.7	12.33	0.470	0.01579	40.0	0.560	0.856
		1626	11.8	14.26	0.480	0.01539	40.4	0.604	0.850

TABLE 1 - CONCLUDED

MODEL	$\bar{x}_o$	P_o (PSIA)	M_∞	$Re_{\infty,\ell} \times 10^{-6}$	P_b/P_∞	P_o'/P_o	ν (HZ)	$-C_{m_{\dot\theta}}$	$-C_{m_\theta}$
B4	0.653	816	11.3	7.51	0.499	0.01686	33.2	0.508	0.029
		1002	11.5	9.00	0.505	0.01649	33.2	0.513	0.021
		1192	11.6	10.66	0.507	0.01606	33.1	0.527	0.014
		1392	11.7	12.30	0.505	0.01565	33.1	0.521	0.010
		1606	11.8	14.13	0.526	0.01535	33.1	0.578	0.002
B7	0.50	797	11.3	7.29	0.499	0.01688	37.7	0.449	0.542
		992	11.5	8.95	0.474	0.01642	38.0	0.435	0.548
		1199	11.6	10.71	0.442	0.01590	38.2	0.475	0.541
		1405	11.7	12.45	0.425	0.01556	38.4	0.434	0.537
		1630	11.8	14.31	0.413	0.01525	38.5	0.479	0.488
B7	0.653	797	11.3	7.29	0.493	0.01699	33.1	0.364	0.037
		1007	11.5	9.04	0.462	0.01655	33.1	0.366	0.033
		1187	11.6	10.57	0.442	0.01614	33.1	0.346	0.026
		1189	11.6	10.57	0.441	0.01617	33.1	0.354	0.023
		1402	11.7	12.42	0.420	0.01568	33.0	0.397	0.013
		1606	11.8	14.13	0.410	0.01533	33.1	0.393	0.016

$\ell = 9.000$ IN.

MODEL	a/b	ℓ/d	a/d
B1	1.0	3.67	0.50
B3	3.0	3.67	0.87
B4	6.0	3.67	1.22
B7	1.7	3.67	0.70

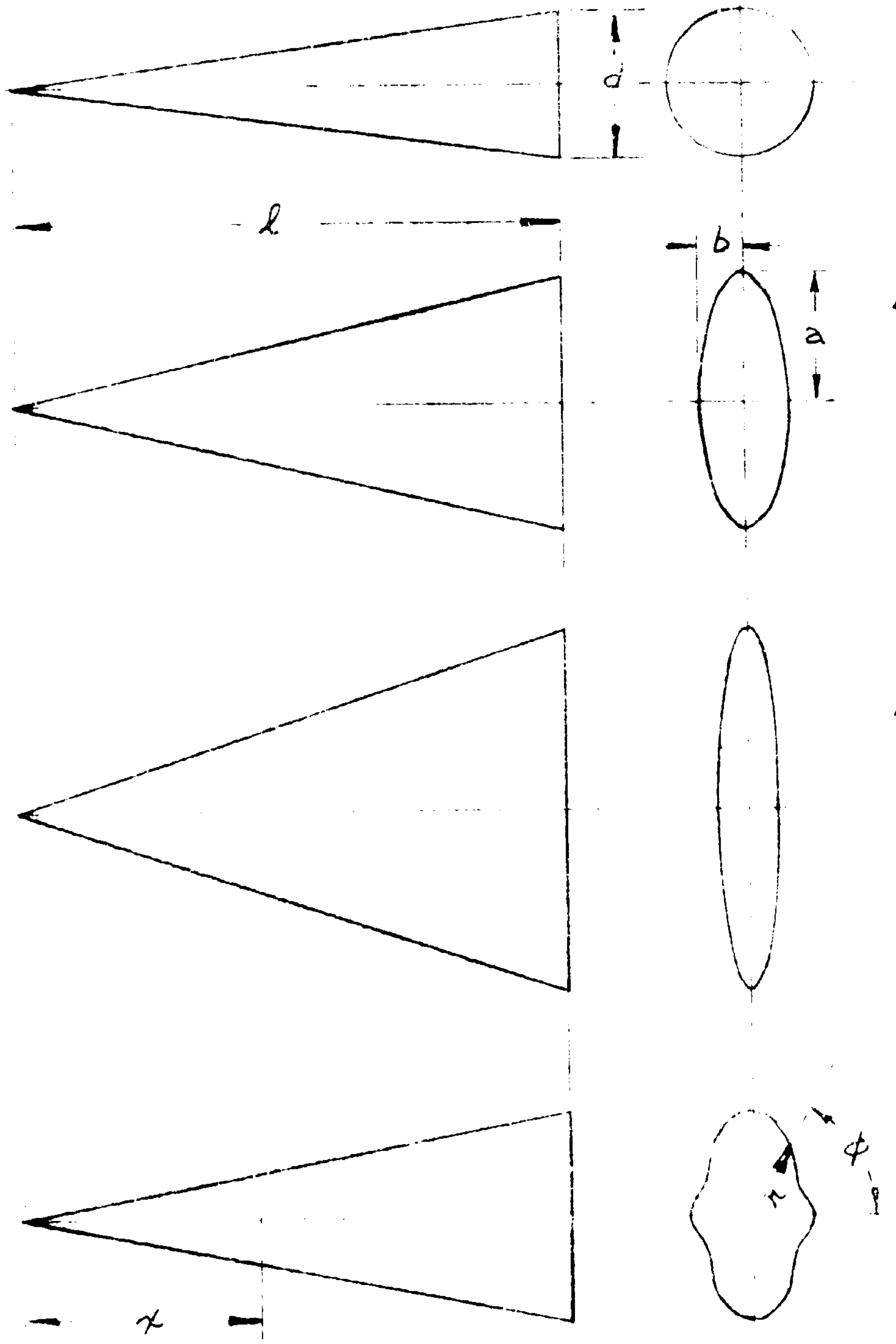

FOR B7 ONLY: $r/x = 0.661\,(0.2 - 0.06\cos 2\phi + 0.03\cos 4\phi)$

$a = [r]_{\phi = 90^\circ}$; $b = [r]_{\phi = 0^\circ}$

FIG. 1 GEOMETRIC PARAMETERS OF MODELS

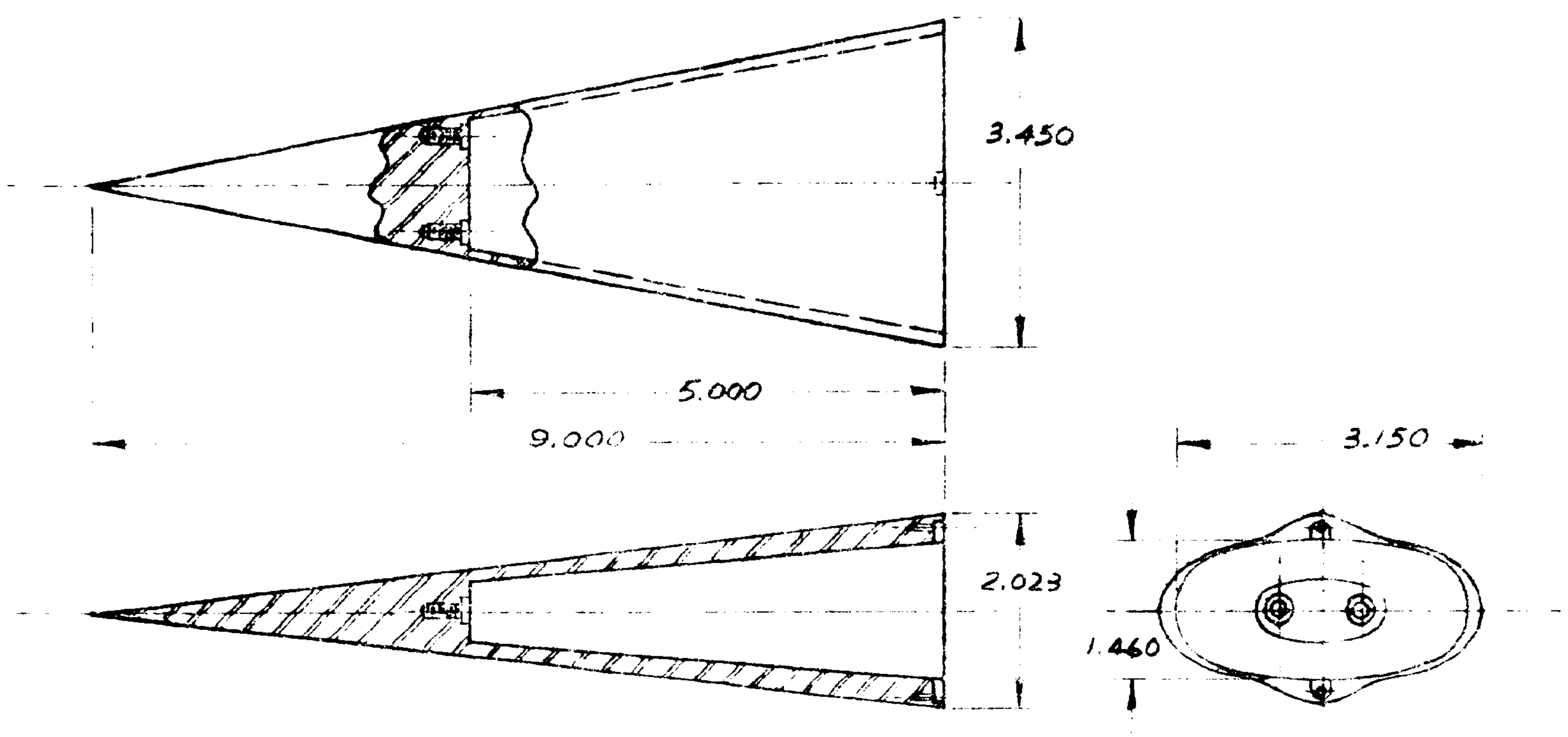

ALL DIMENSIONS IN INCHES

MATERIAL: STAINLESS STEEL

FIG. 2 CONSTRUCTIONAL DETAILS OF MODELS (B7, TYPICAL)

B1 B3 B4 B7

FIG. 3 VIEW OF BASE OF MODELS

FIG. 4 STING AND MODEL ADAPTORS

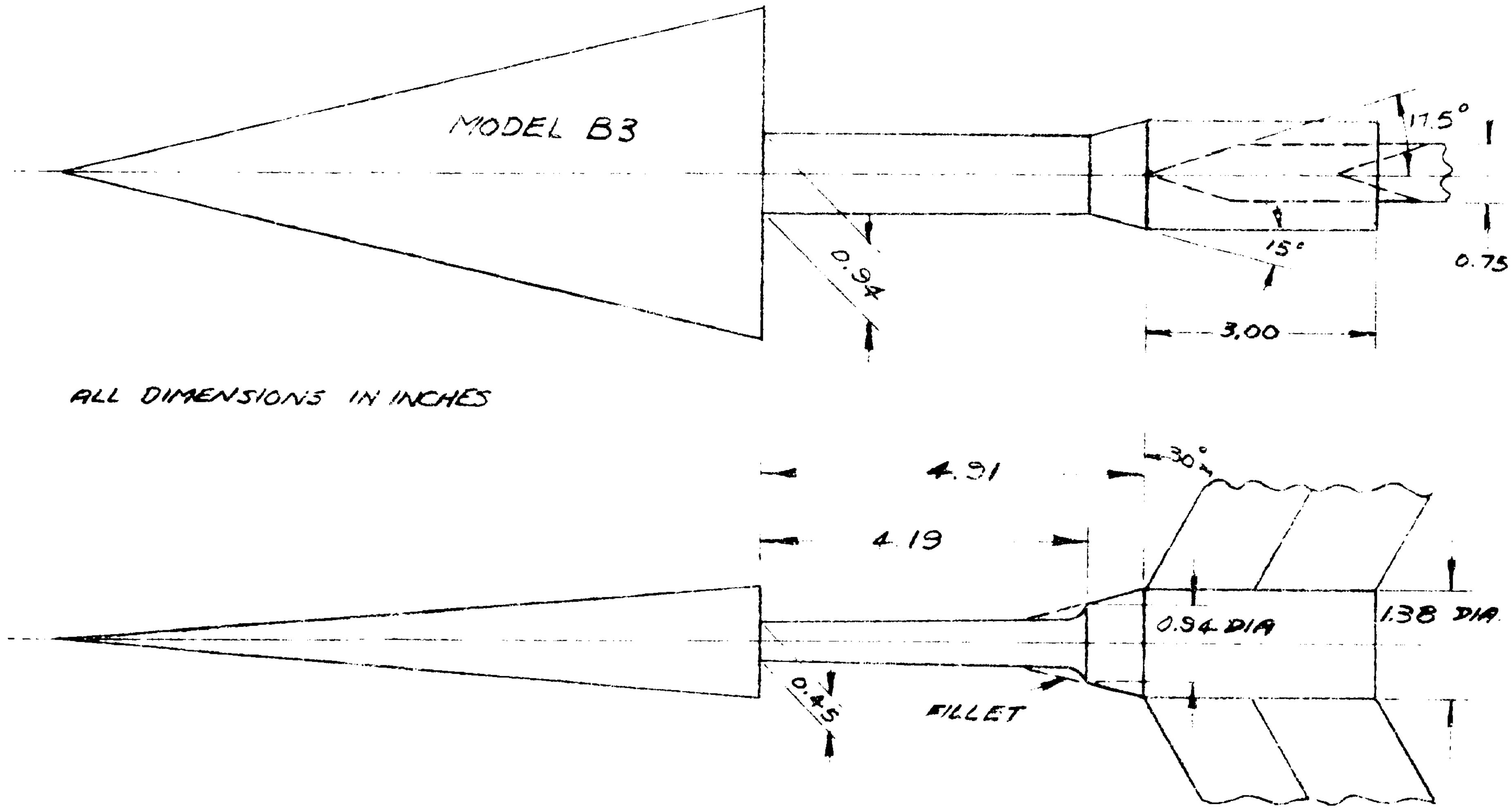

ALL DIMENSIONS IN INCHES

FIG. 5 STING AND SUPPORT DIMENSIONS

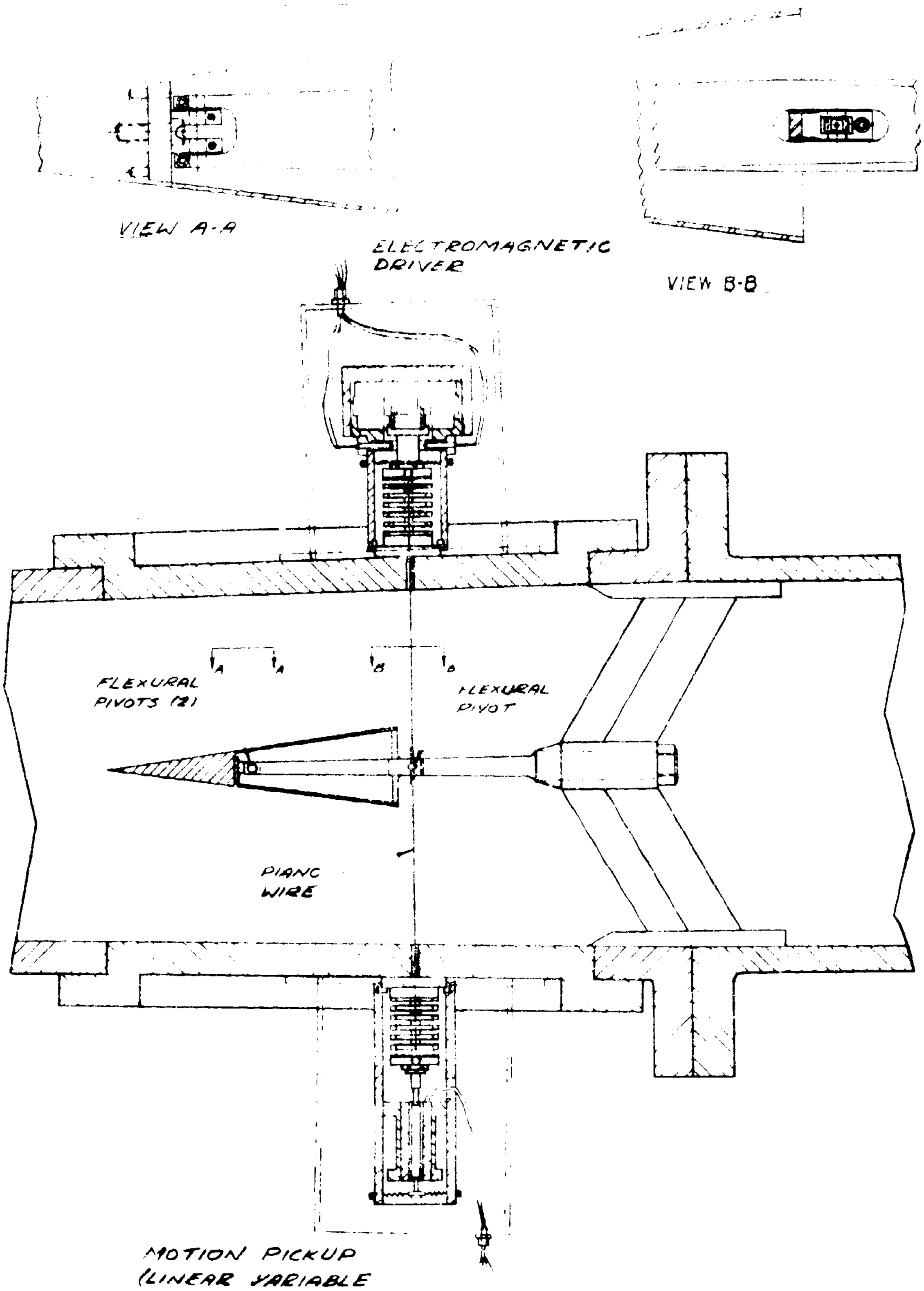

Fig. 6 SCHEMATIC OF OSCILLATORY APPARATUS AND MODEL IN THE HYPERSONIC WIND TUNNEL

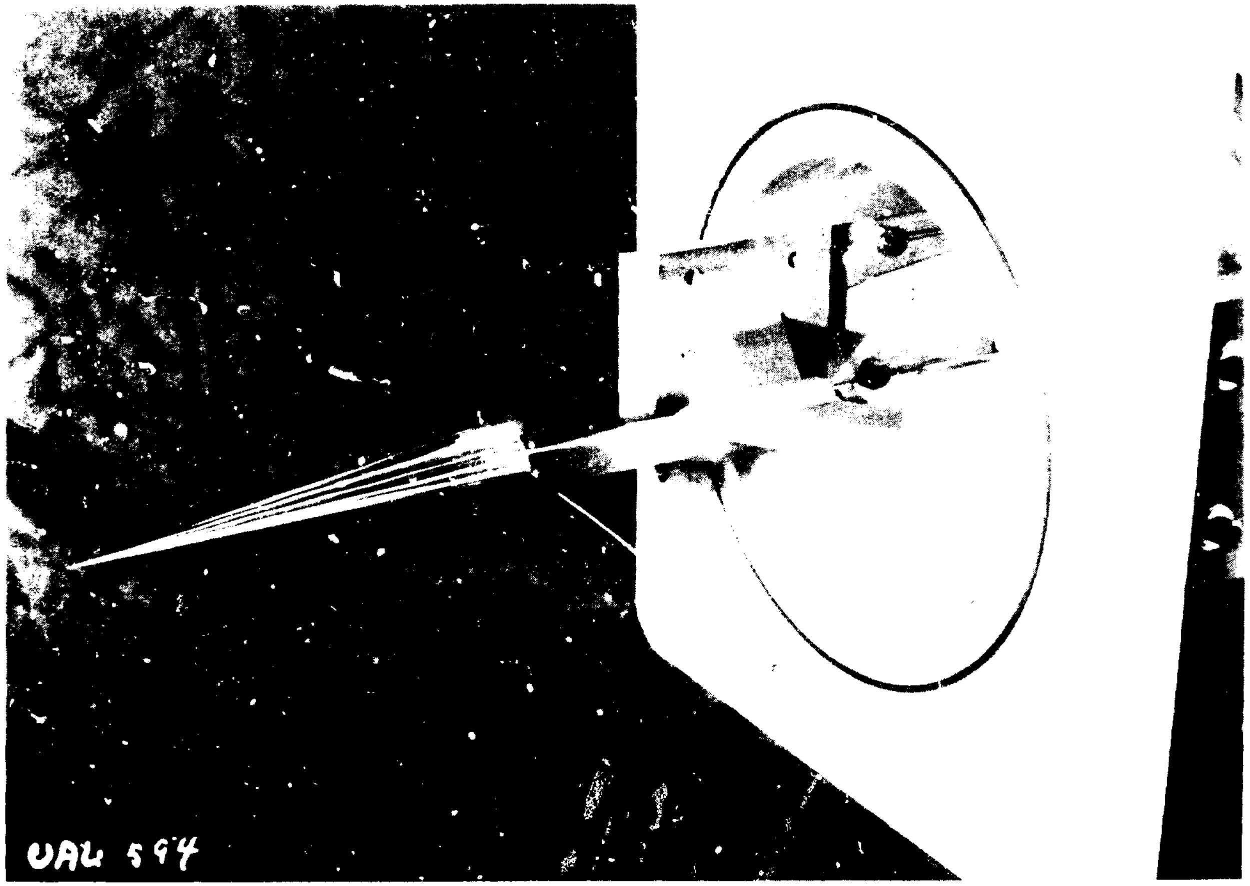

FIG. 7 MODEL MOUNTED ON STING AND SUPPORT IN TRANSITION SECTION OF HYPERSONIC WIND TUNNEL

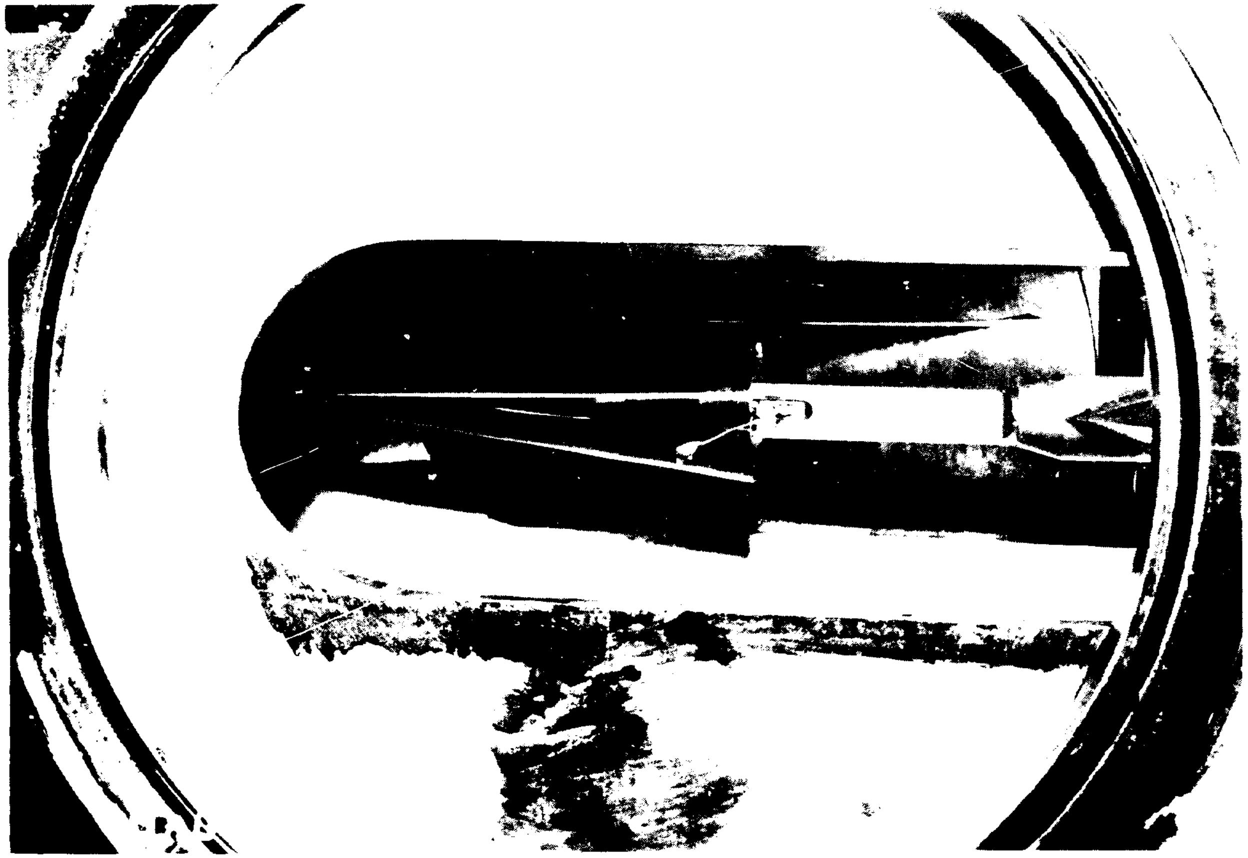

FIG. 8 MODEL MOUNTED IN TEST SECTION

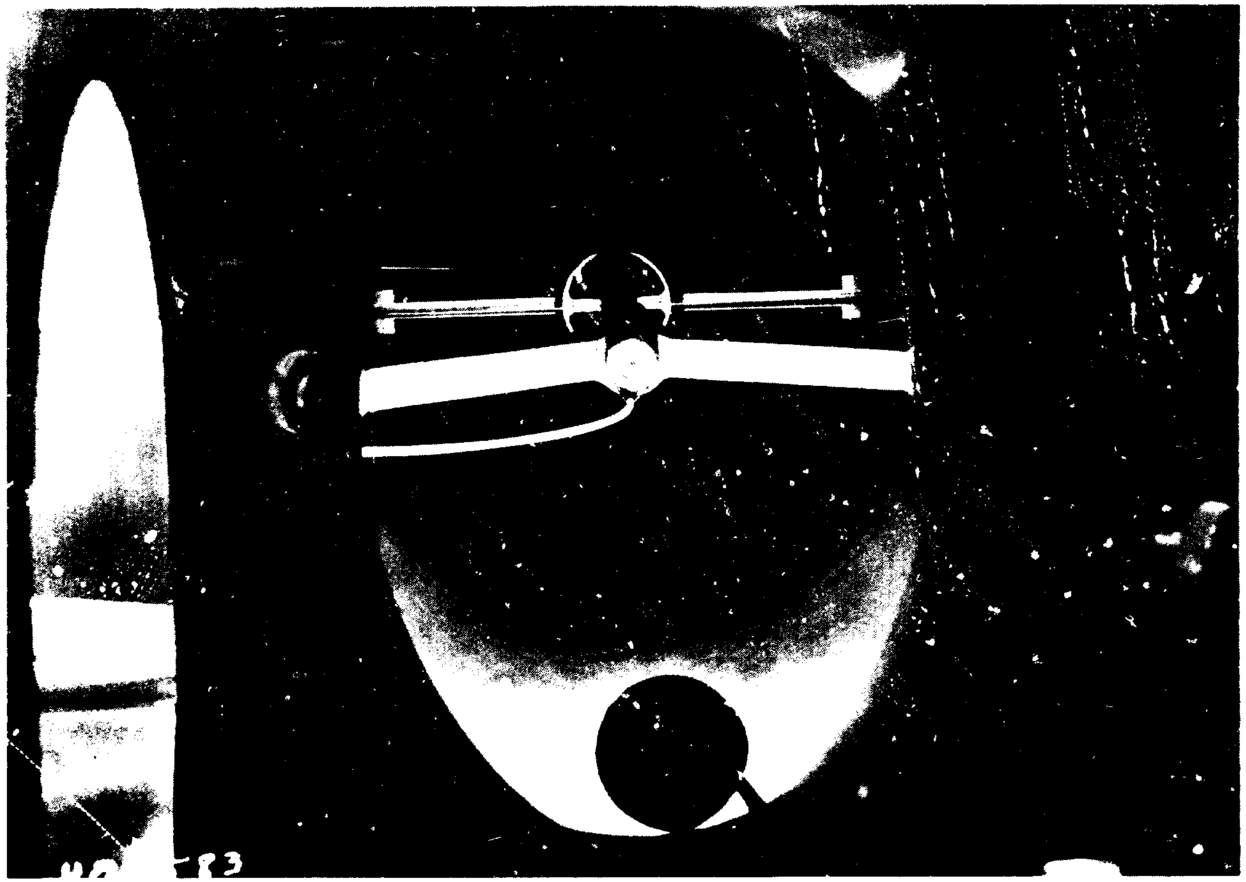

FIG. 9 MODEL MOUNTED IN NOZZLE, LOOKING UPSTREAM

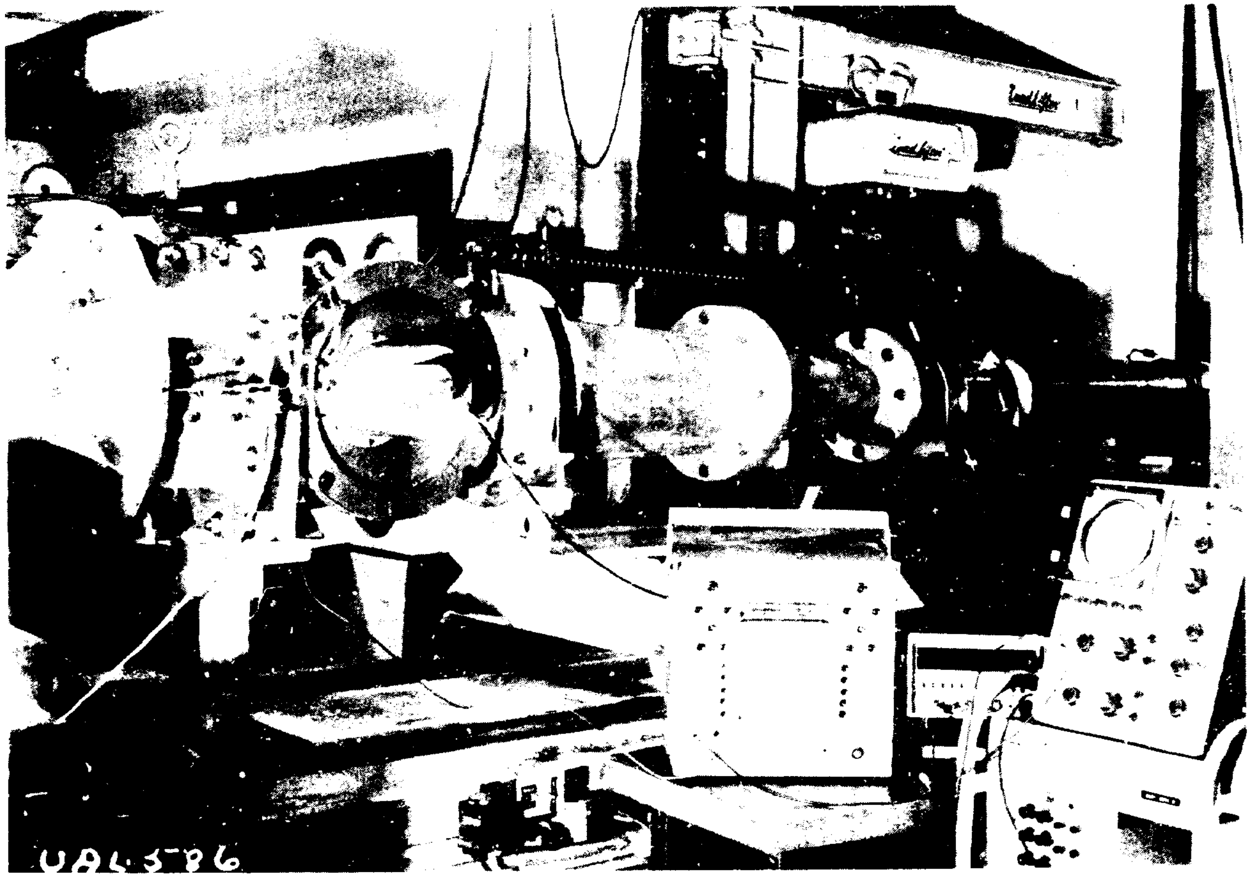

FIG. 10 WIND TUNNEL AND PART OF INSTRUMENTATION

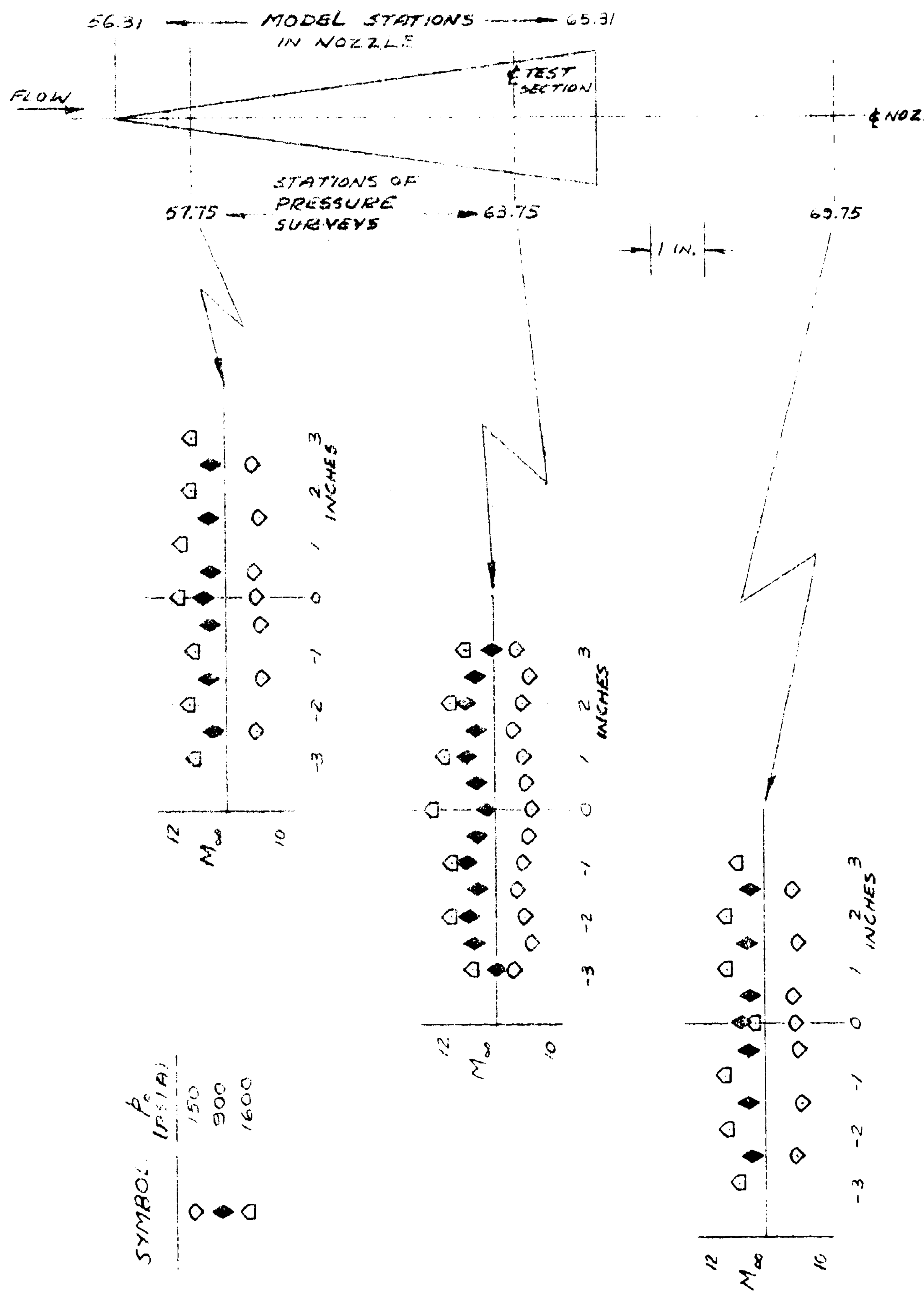

FIG. 11 MACH NUMBER DISTRIBUTIONS IN PLANE OF OSCILLATION

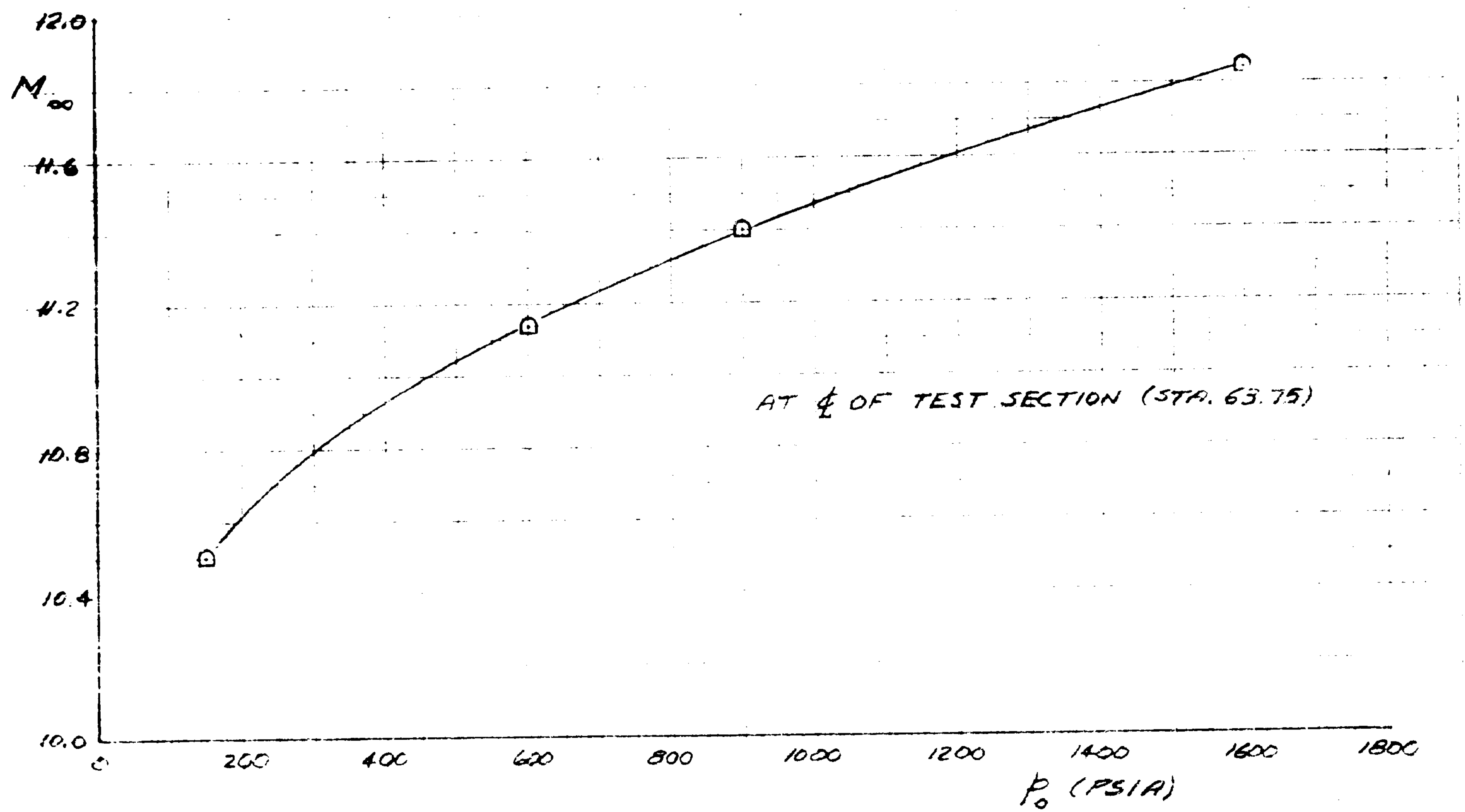

FIG. 12 EFFECT OF p_o ON MEAN MACH NUMBER

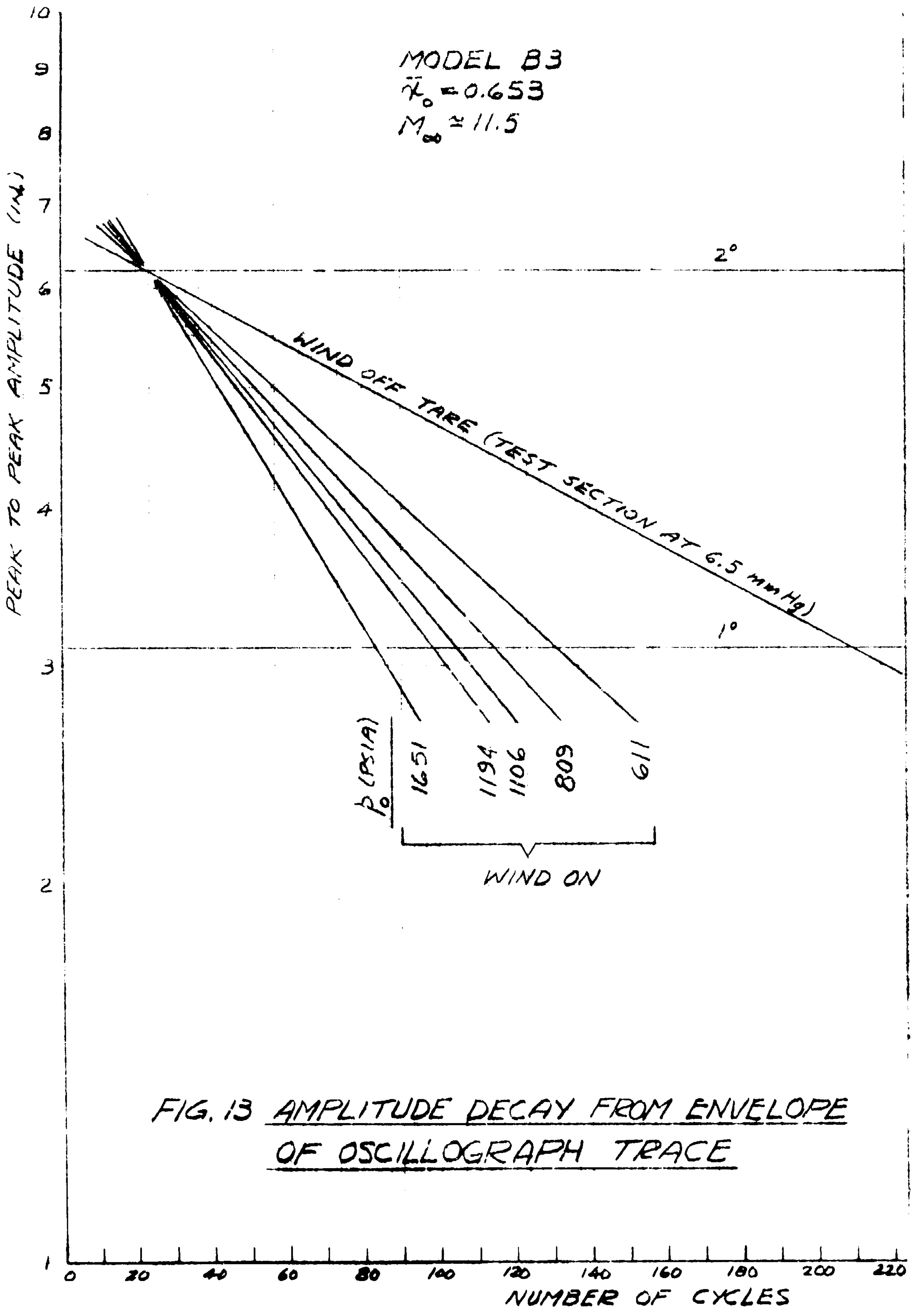

FIG. 13 AMPLITUDE DECAY FROM ENVELOPE OF OSCILLOGRAPH TRACE

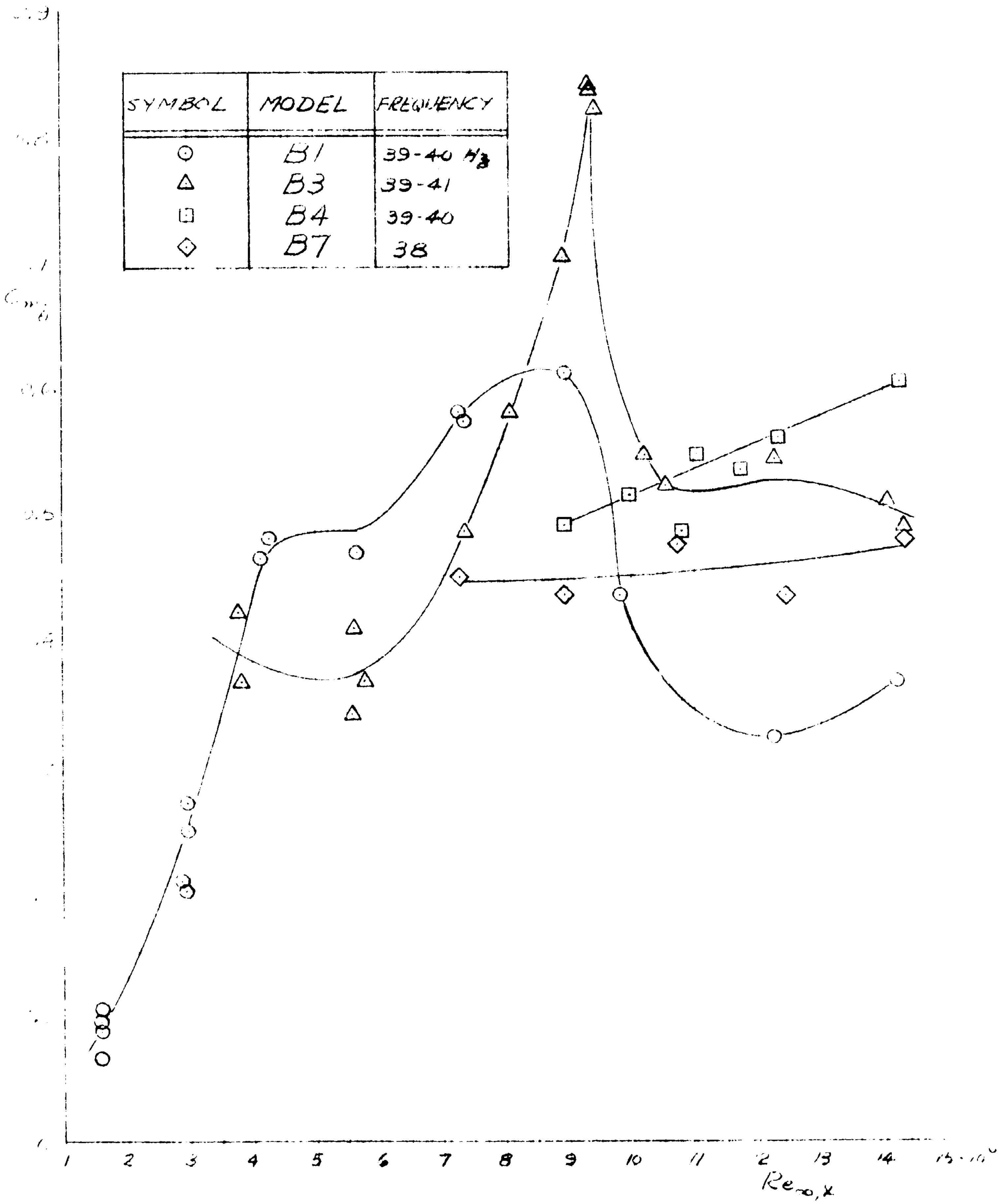

FIG. 14 DAMPING-IN-PITCH DERIVATIVE

$\bar{x}_o = 0.50$, $M_\infty \simeq 11.3$

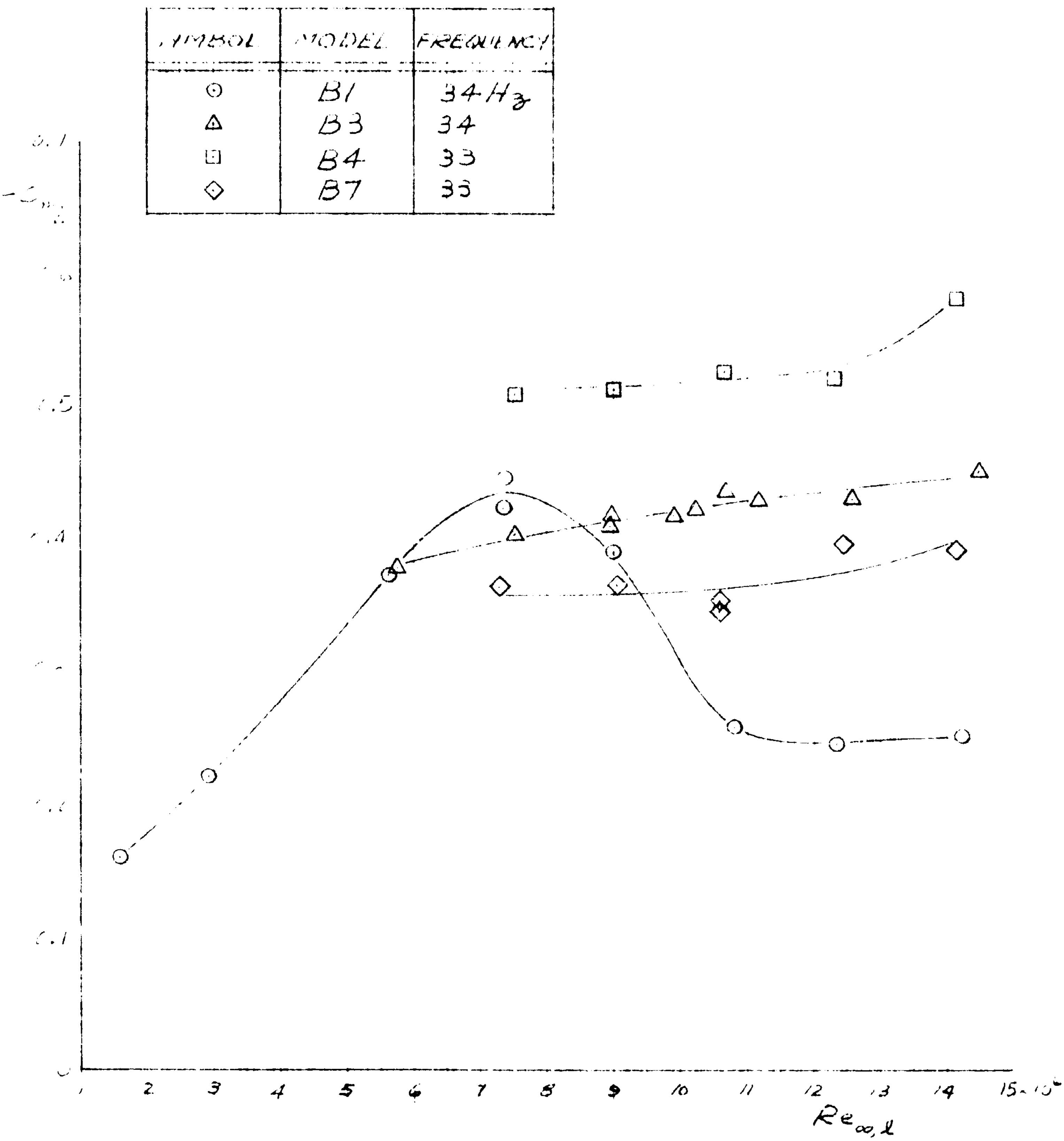

FIG. 15 DAMPING-IN-PITCH DERIVATIVE

$\bar{x}_o = 0.653$, $M_\infty \simeq 11.3$

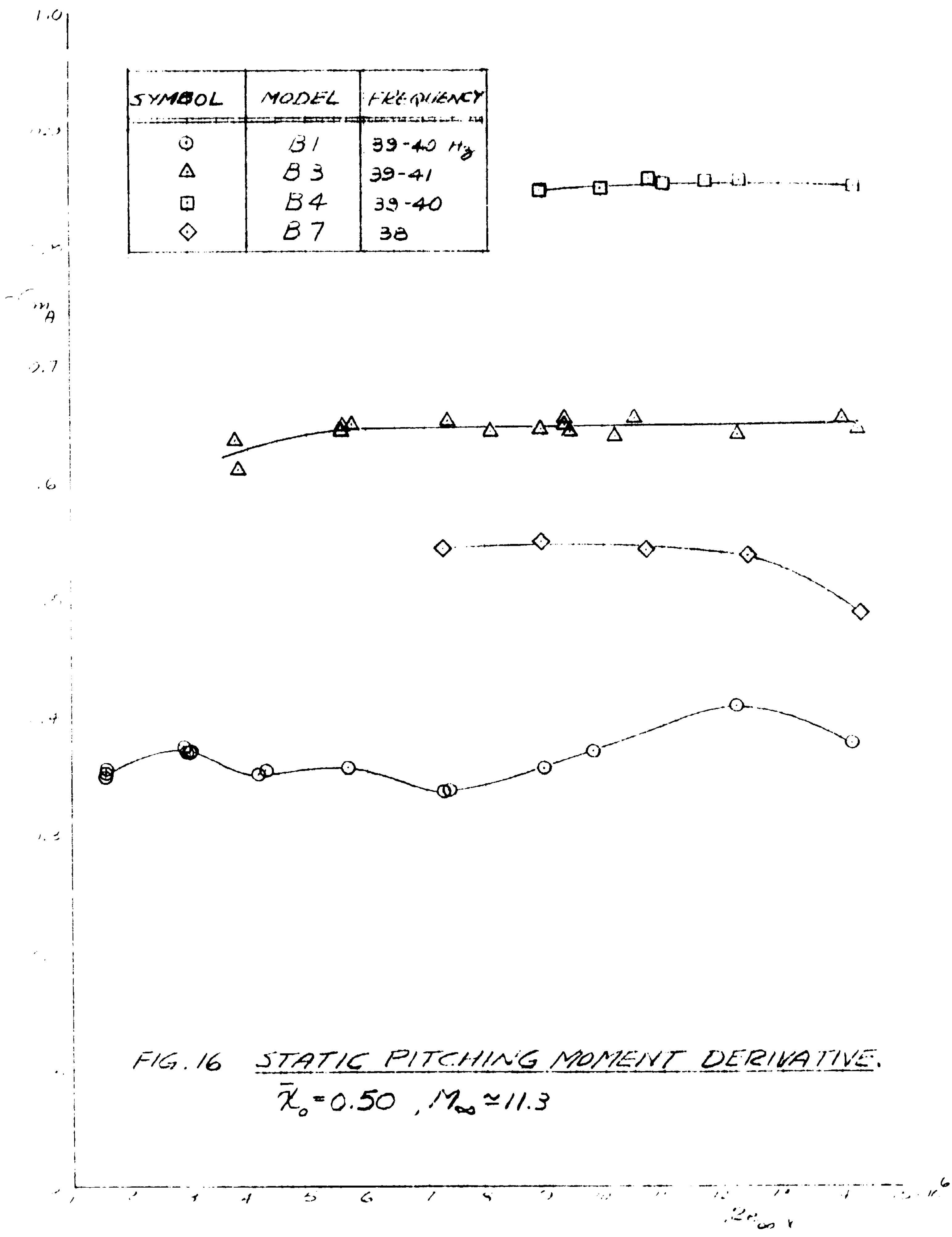

FIG. 16 STATIC PITCHING MOMENT DERIVATIVE.

$\bar{x}_0 = 0.50$, $M_\infty \simeq 11.3$

SYMBOL	MODEL	FREQUENCY
⊙	B1	34 Hz
△	B3	34
⊡	B4	33
◇	B7	33

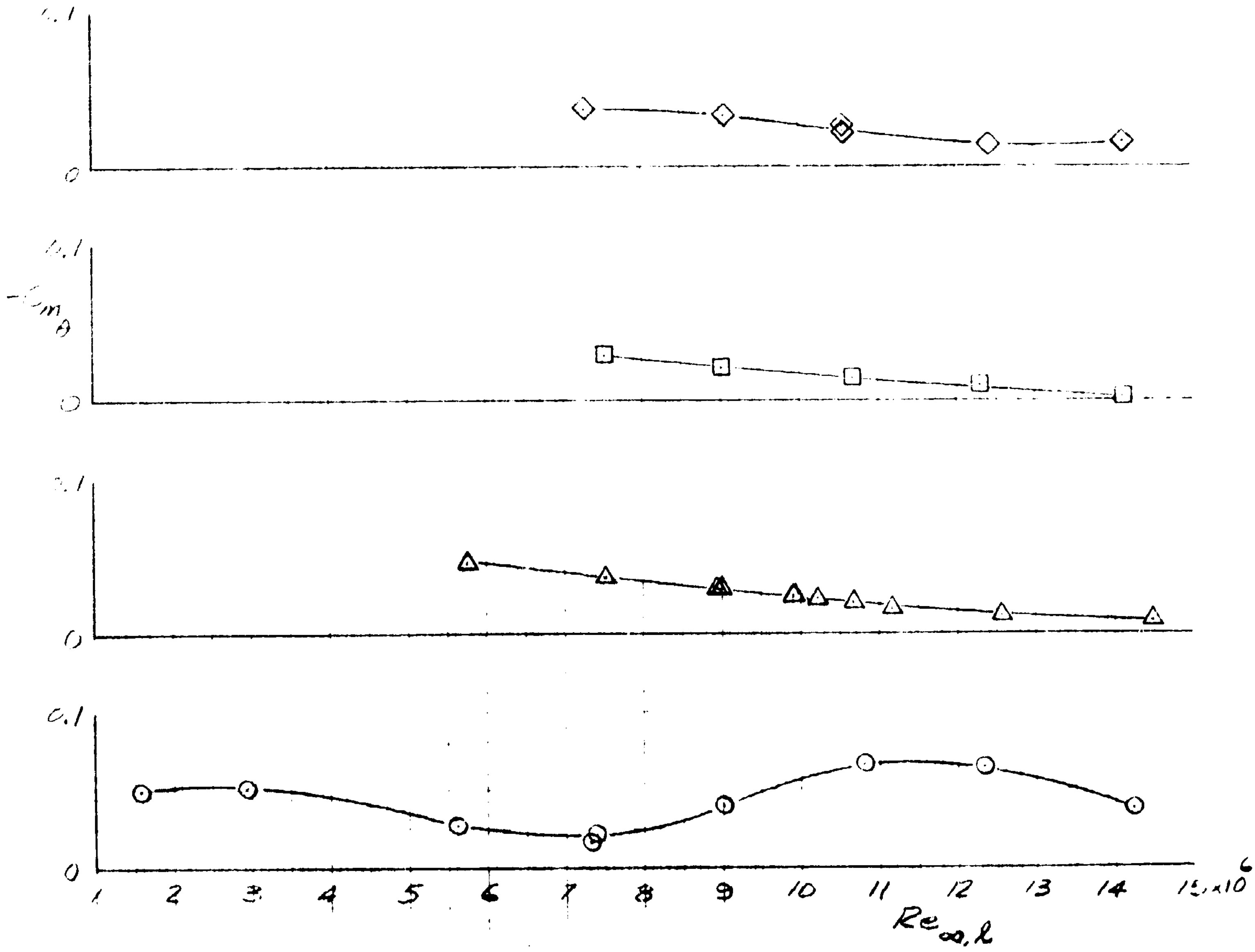

FIG. 17 STATIC PITCHING MOMENT DERIVATIVE

$\bar{x}_0 = 0.653$, $M_\infty \approx 11.3$

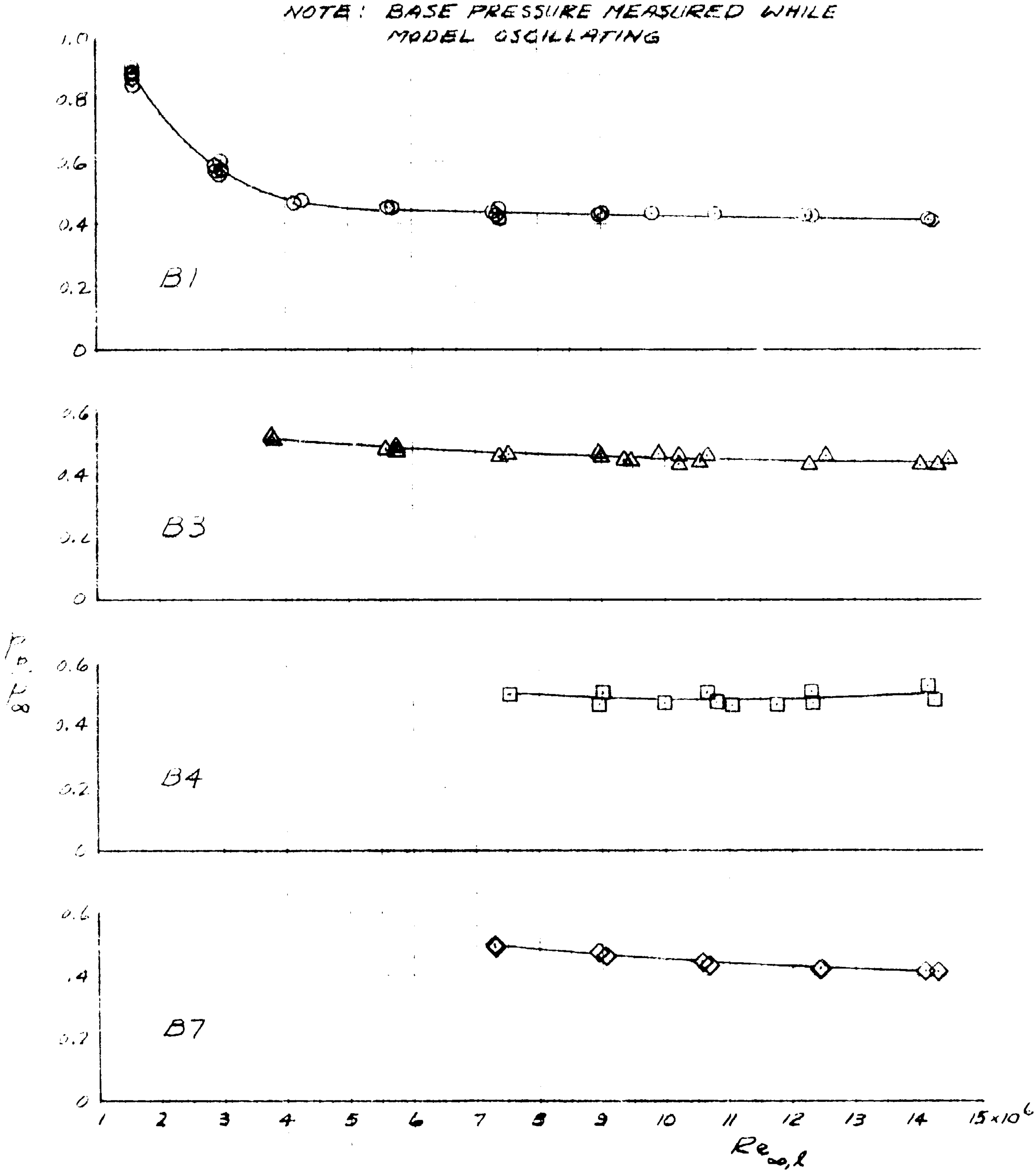

FIG. 18 MEAN BASE PRESSURE, $M_\infty \doteq 11.3$

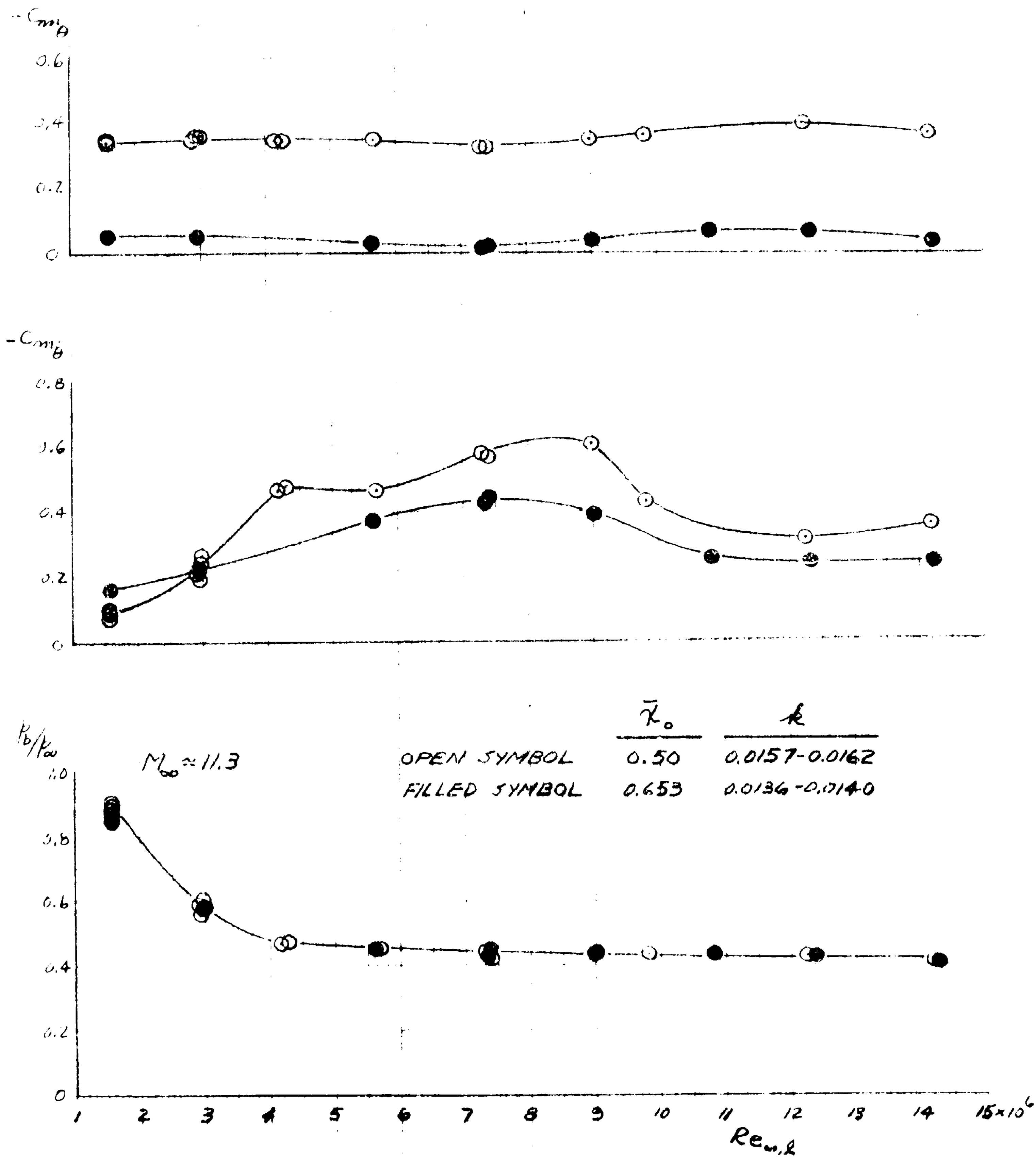

FIG. 19 RESULTS FOR MODEL B1

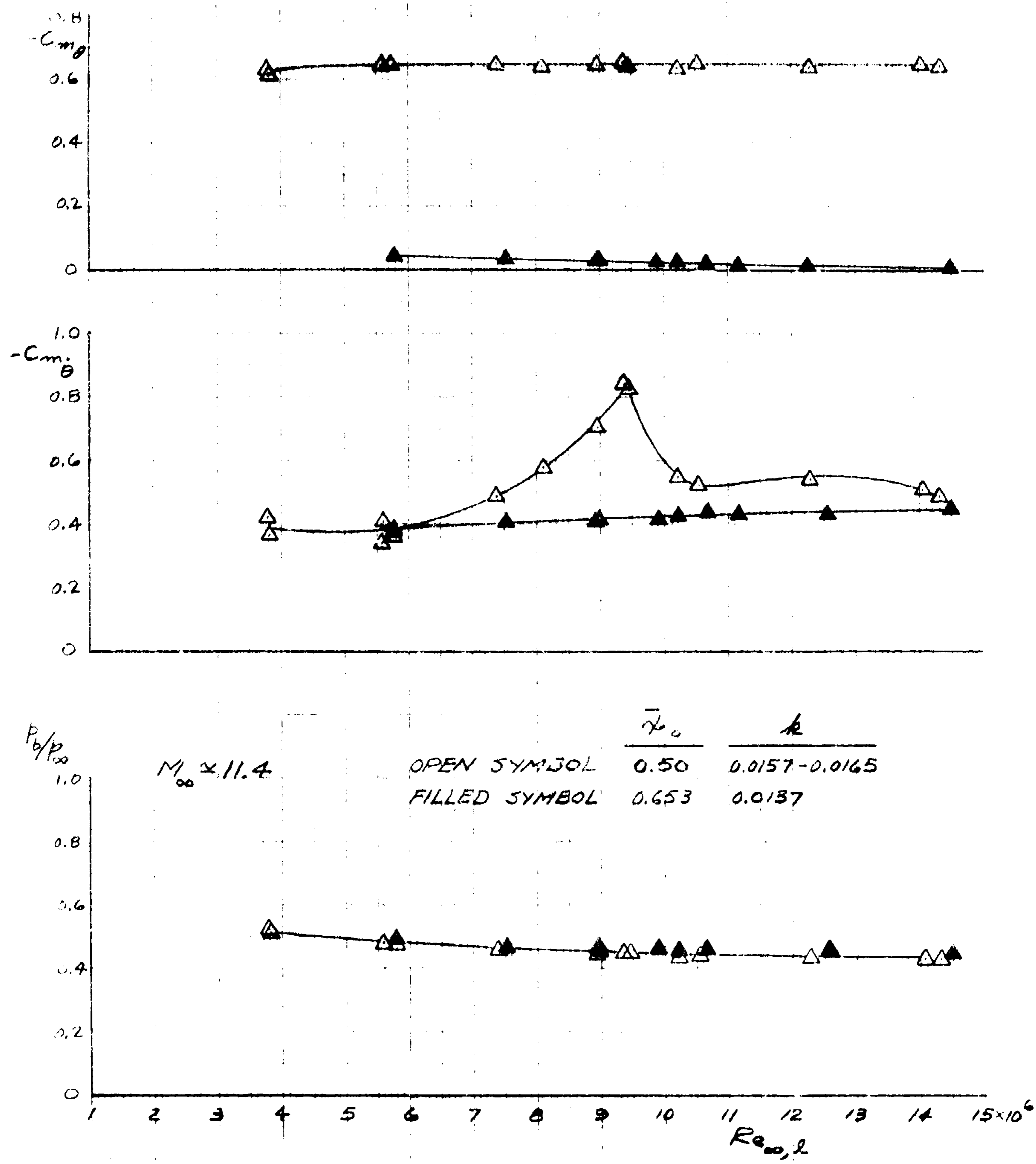

FIG. 20 RESULTS FOR MODEL B3

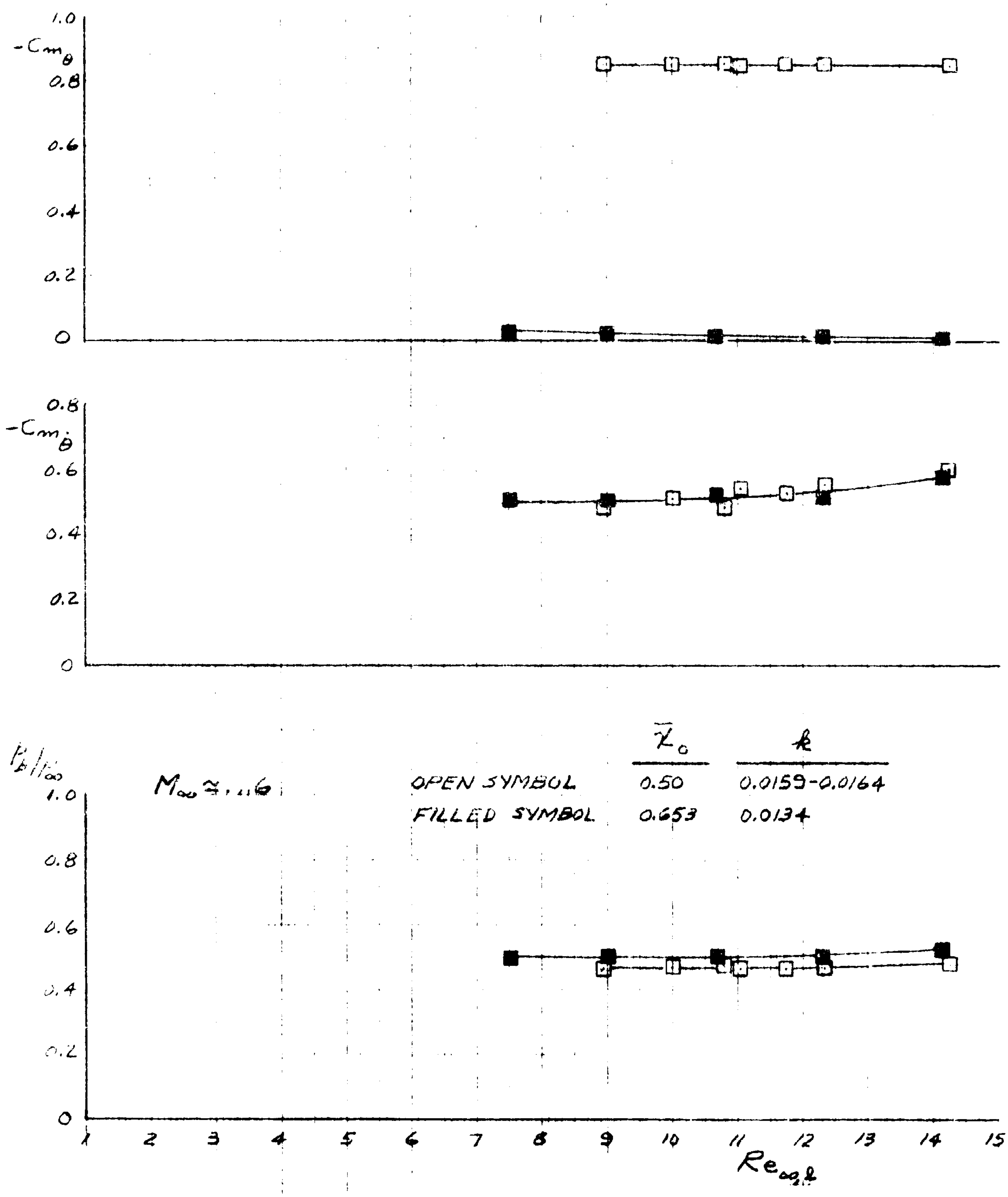

FIG. 21 RESULTS FOR MODEL B4

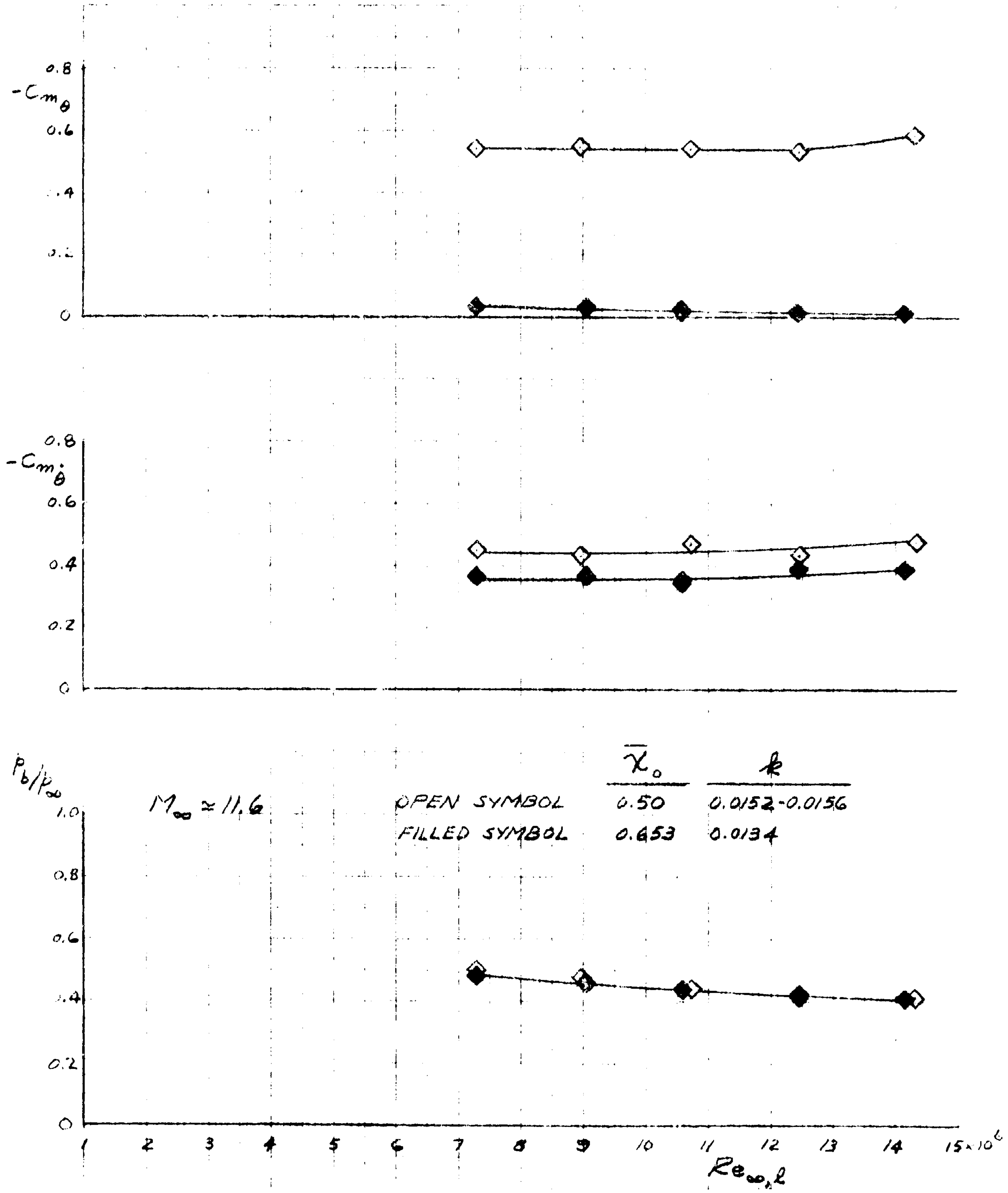

FIG. 22 RESULTS FOR MODEL B7

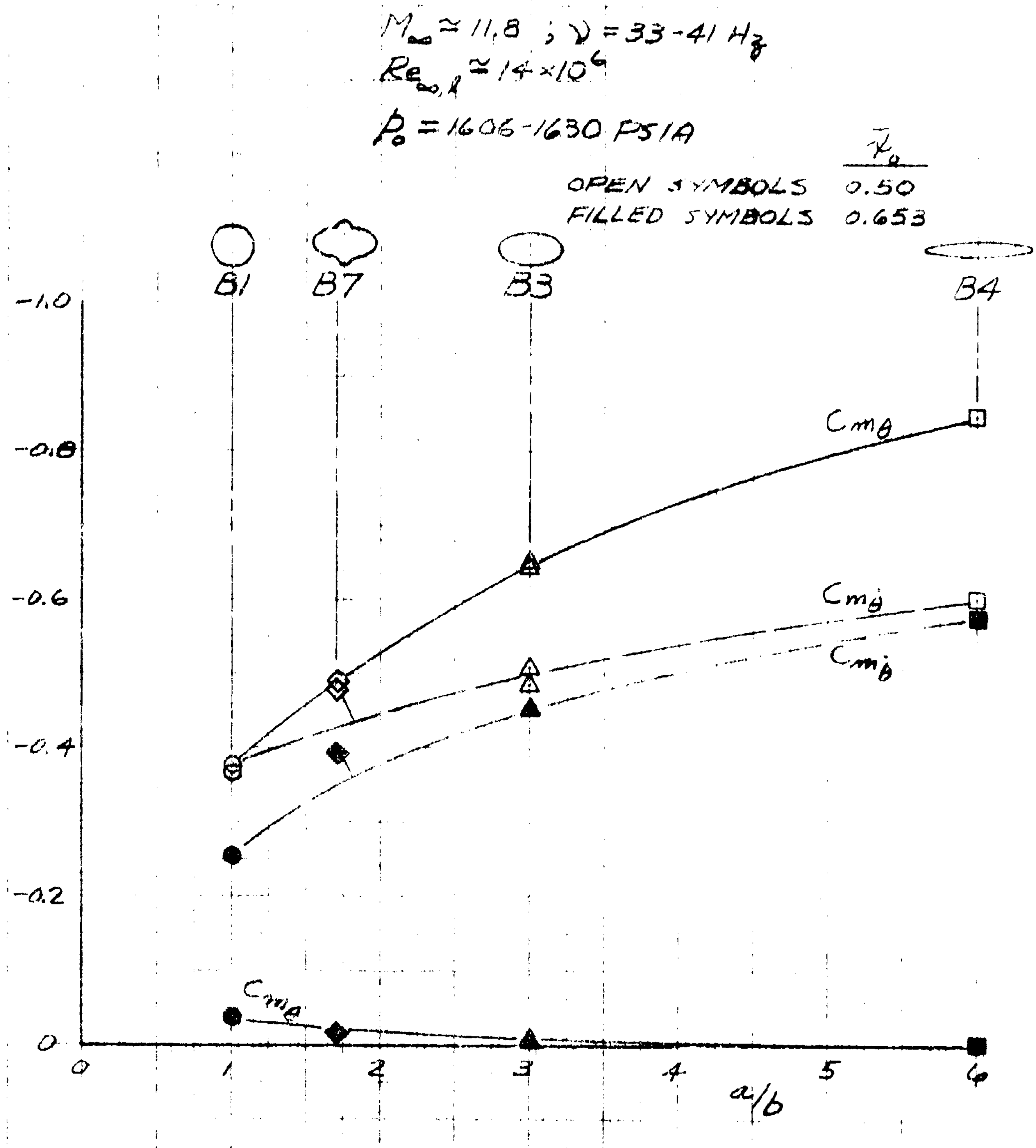

FIG. 23 EFFECT OF AXIS RATIO ON C_{m_θ} AND $C_{m_{\dot\theta}}$
(DERIVATIVES ABOUT EXPERIMENTAL AXES)

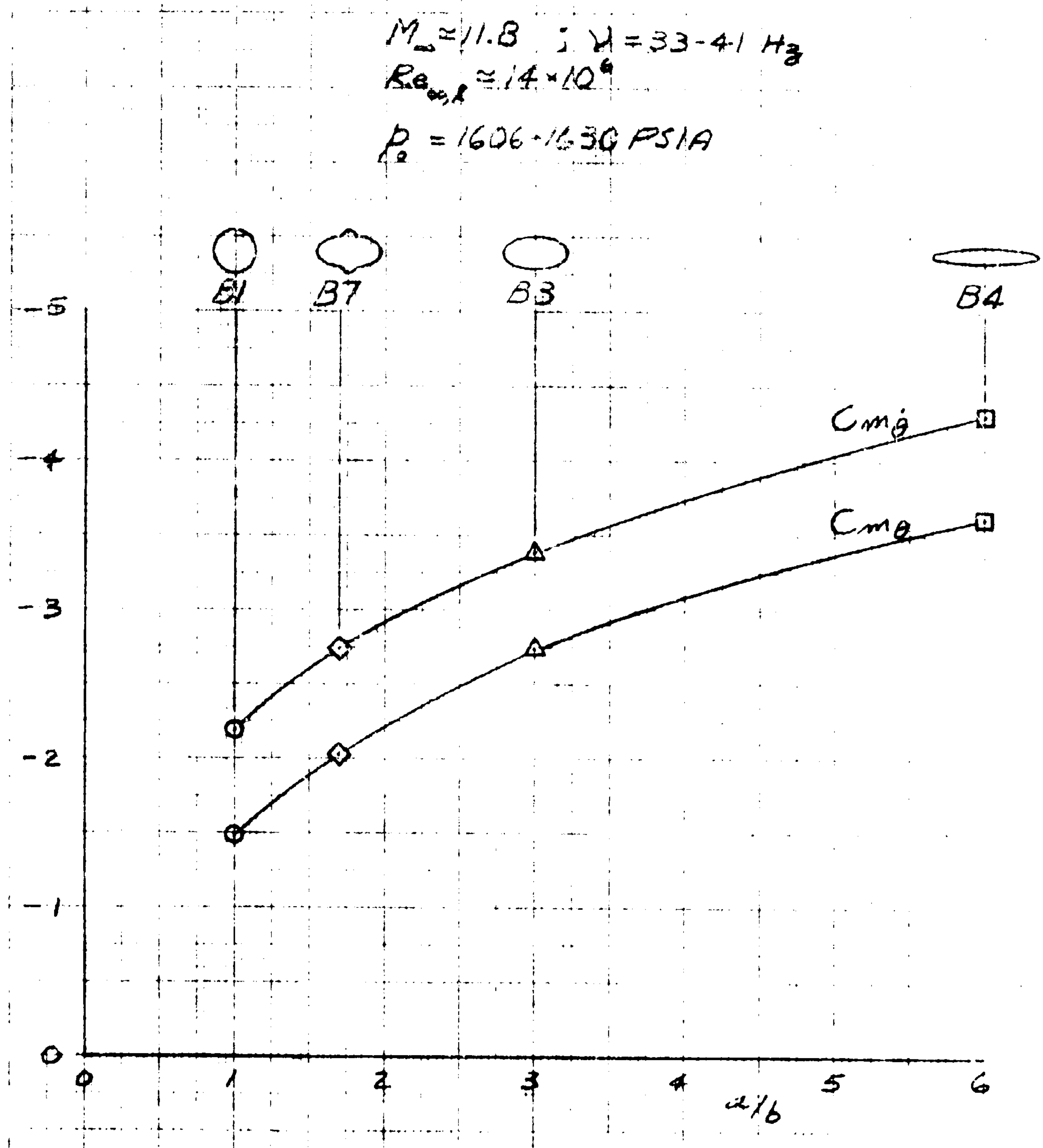

FIG.24 PITCHING MOMENT DERIVATIVES ABOUT APEX

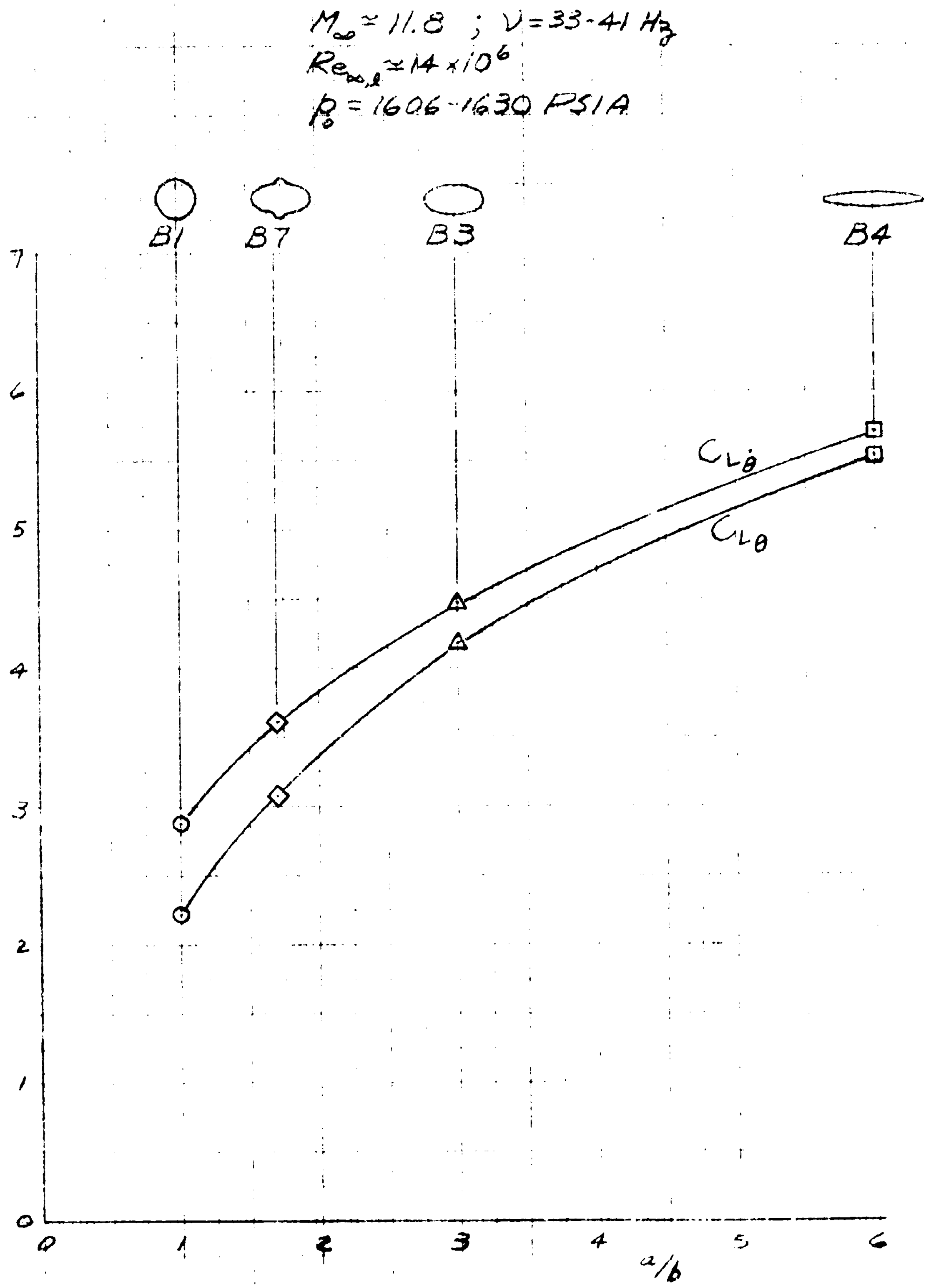

FIG. 25 LIFT DERIVATIVES ABOUT APEX

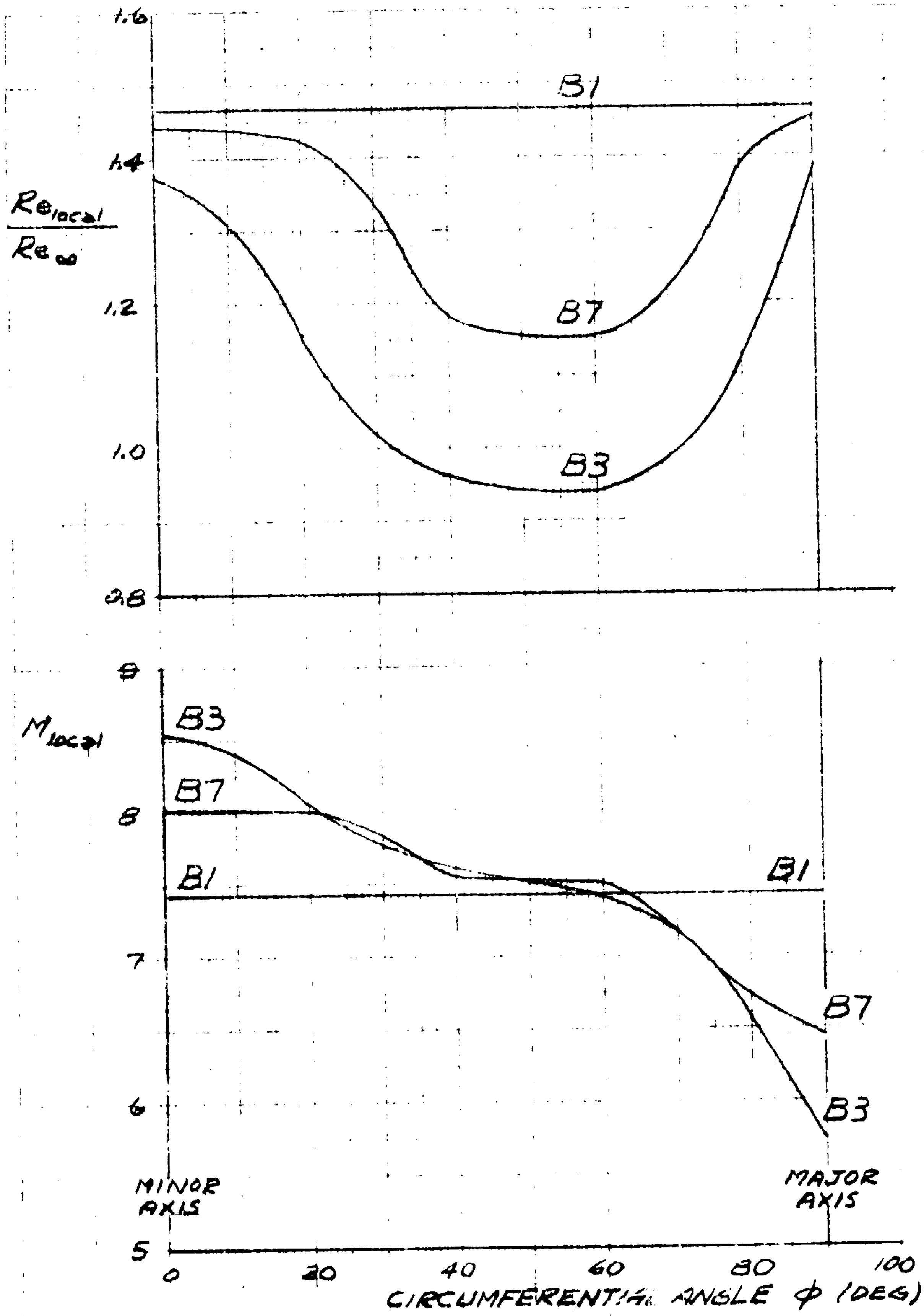

FIG. 26 CIRCUMFERENTIAL DISTRIBUTION OF THE REYNOLDS NUMBER RATIO AND THE LOCAL MACH NUMBER (CALCULATED BY THE METHODS OF REF. 2)

× ACTUAL VALUES OF Re_{local}/Re_{∞} CALCULATED (BY METHODS OF REF. 2) AT THE INTERSECTION OF MODEL SURFACE AND THE MINOR AXIS, AND PLOTTED AT THE θ_c OF THE CORRESPONDING INSCRIBED CIRCULAR CONE

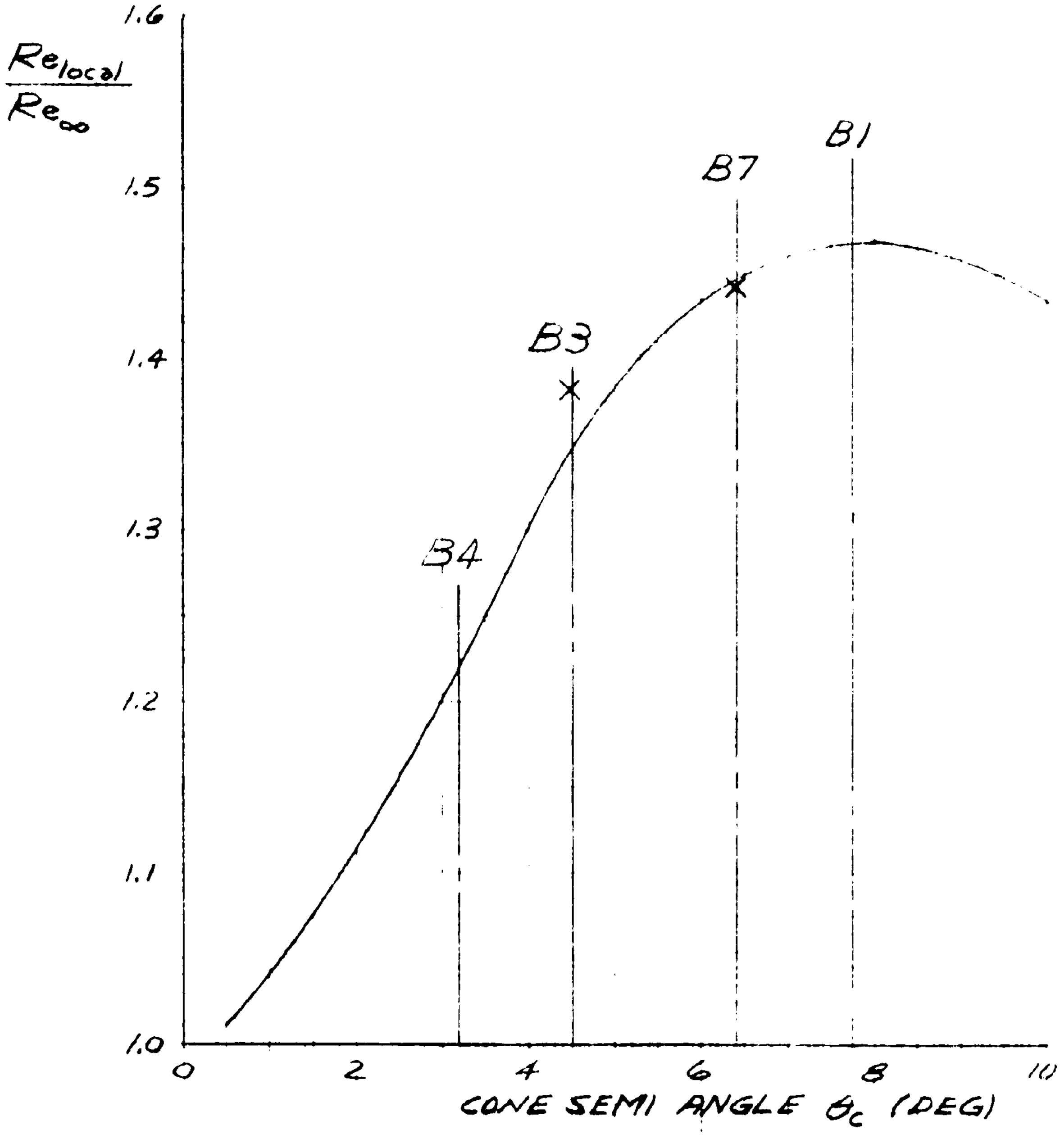

FIG. 27 RATIO OF LOCAL TO FREE-STREAM REYNOLDS NUMBER FOR CIRCULAR CONES AT $M_{\infty} = 11$ AND $\gamma = 5/3$

END

DATE

FILMED

OCT. 24 1972